Anti-reflective coatings: A critical, in-depth review

DATASET *in* ENERGY & ENVIRONMENTAL SCIENCE · JANUARY 2011

Impact Factor: 20.52

4 AUTHORS, INCLUDING:

Hemant K Raut
National University of Singapore
14 PUBLICATIONS **229** CITATIONS
SEE PROFILE

Anand Ganesh Venkatesan
Singapore University of Technology and De…
18 PUBLICATIONS **544** CITATIONS
SEE PROFILE

Energy & Environmental Science

Cite this: *Energy Environ. Sci.*, 2011, **4**, 3779

www.rsc.org/ees

REVIEW

Anti-reflective coatings: A critical, in-depth review

Hemant Kumar Raut,*[a] V. Anand Ganesh,[a] A. Sreekumaran Nair[b] and Seeram Ramakrishna*[acd]

Received 15th March 2011, Accepted 7th June 2011
DOI: 10.1039/c1ee01297e

Anti-reflective coatings (ARCs) have evolved into highly effective reflectance and glare reducing components for various optical and opto-electrical equipments. Extensive research in optical and biological reflectance minimization as well as the emergence of nanotechnology over the years has contributed to the enhancement of ARCs in a major way. In this study the prime objective is to give a comprehensive idea of the ARCs right from their inception, as they were originally conceptualized by the pioneers and lay down the basic concepts and strategies adopted to minimize reflectance. The different types of ARCs are also described in greater detail and the state-of-the-art fabrication techniques have been fully illustrated. The inspiration that ARCs derive from nature ('*biomimetics*') has been an area of major research and is discussed at length. The various materials that have been reportedly used in fabricating the ARCs have also been brought into sharp focus. An account of application of ARCs on solar cells and modules, contemporary research and associated challenges are presented in the end to facilitate a universal understanding of the ARCs and encourage future research.

1. Introduction

Light transmission and production have been an area of profound intricacy that baffled scientists and inquisitives since the proverbial Newtonian era. The conclusive explanation of structural colour of silverfish and peacock offered by Hooke[1] and Newton[2] and later, of the membranous wings of many insects by Goureau,[3] modified the popular notion of coloration. Interaction of light with different structures received a lot of research attention and major breakthroughs such as explanation of highly metallic to dull green colour of beetle's cuticle and wings of butterfly *Arhopala Micale* (interference), discovery of zero order gratings in the cornea of *Zalea Minor* (Diptera) making it highly anti-reflective (diffraction) and the bluishness of the skin of *Octopus Bimaculatus* (scattering), to name a few, were accomplished.[3] It was this relentless quest for understanding nature's optical strategy for imparting conspicuousness or camouflaging to the astonishingly diverse array of biological species that led to the conceptualization of anti-reflectivity. The iridescent blue of *Morpho Rhentenor* butterfly wings which are prominent from great distance and the cornea of nocturnal moths that remain absolutely lustreless to disguise predators were analyzed for the first time with the aid of ultra-powerful scanning electron microscopy. The cuticular protuberances called corneal nipple array on the surface of these species held the key to a great deal of research and commercialization that ensued thereafter.

In the world of physical sciences, the idea of anti-reflective coatings was quite incidentally construed by Lord Rayleigh (John Strutt) in the 19th century when he observed the tarnishing on a glass increasing its transmittance instead of reducing it. This led to the strategy of achieving anti reflectivity by gradually varying the refractive index. However, the actual anti-reflective coatings were produced by Fraunhofer[4] in 1817 when he noticed that reflection was reduced as a result of etching a surface in an atmosphere of sulphur and nitric acid vapours.

The ever growing demand of optical and opto-electronic equipments in areas as diverse as space exploration to consumer electronics has led to the search for ways to maximize light collection efficiency. Anti-reflective coatings on top glass cover of the solar panel have served quite well in this regard, by bringing about better transmission and glare reduction. As for solar cells, reflectance reduction is achieved by silicon nitride or titanium dioxide coatings of nanometre scales produced by PECVD discussed later. Additionally, textured front surface of solar cells especially in mono-crystalline silicon helps increase light coupled into the cell. Moreover, as the world is witnessing the long overdue transition to alternative sources of energy especially solar; low conversion efficiency due to reflection losses in the conventional photovoltaic modules poses a major bottleneck. It has been reported that a normal solar panel absorbs approximately 25% of the incident solar radiation, thus, reflecting a third of the incident radiation which could otherwise have contributed to the overall efficiency. Moreover, conventional solar panels require an integrated mechanized tracking system that keeps

[a]*Department of Mechanical Engineering, National University of Singapore, Singapore, 117574, Singapore. E-mail: hemantraut@nus.edu.sg; seeram@nus.edu.sg*
[b]*Healthcare and Energy Materials Laboratory, National University of Singapore, 2 Engineering Drive 3, Singapore; Tel: +6516 8596*
[c]*Institute of Materials Research and Engineering, Singapore, 117602, Singapore*
[d]*King Saud University, Riyadh, 11451, Kingdom of Saudi Arabia*

them aligned to the sun throughout the day though such systems are not mandatory in case of Building Integrated Photovoltaic (BIPV) systems.

To overcome these issues a great many anti-reflective coatings have been commercially manufactured and used though the improvement in overall efficiency gets eclipsed by durability, debonding and high cost issues. In optical equipments especially cameras and eye glasses ARCs have been commercially explored by numerous manufacturers and the results are indeed spectacular. This has led to product manufacturers of LCDs, cathode ray tubes and aerospace sensors take stock and incorporate ARCs to better the performance of their products as well. Yet perfect antireflectivity and exceptional photon collection efficiency even at dusk remain the forte of only a few biological species, easily observed than emulated.

2. Basic concept

The optical phenomenon, reflection is born out of a transition in the medium in which light is travelling. The medium (glass, water, air, *etc.*) is characterized optically by the parameter, refractive index (n) which quantifies the speed of light in the current medium with respect to that in vacuum. Thus, as light travels, eyes can spot an optical disturbance if there is a change in refractive index (RI). It is the Fresnel equation that offers the basic preliminary mathematical model of reflection and refraction. According to Augustin-Jean Fresnel, the fraction of incident light reflected at the interface is measured by reflectance, R and the rest transmitted (refracted) is measured by transmittance, T.

The mathematical model or the vector method[5] to deduce the condition for anti-reflection considers a thin film (RI = n) on a glass substrate (RI = n_s) as shown in Fig. 1 (a) and makes the following assumptions

• The reflected waves have the same intensity and one reflected wave per interface.

• Other optical interactions such as scattering, absorption *etc.* are negligible.

Therefore, from Fig. 1 (a) it's quite obvious that if R_1 and R_2, the two reflected waves, undergo a destructive interference, thereby cancelling each other, there would be no reflection. From this follow the two essential criteria for Anti-Reflection.

• The reflected waves are π radians out of phase or the phase difference, δ is $n\pi/2$.

• The thickness of the film (d) is an odd multiple of $\lambda/4$ where λ is the wavelength of the incident beam.

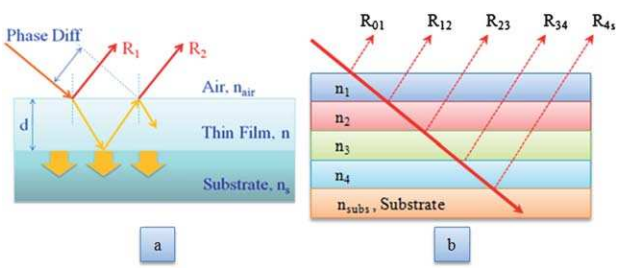

Fig. 1 Propagation of light rays through (a) a single layer film on substrate ($n_s > n$) (b) multilayer film on substrate.

As the equation governing phase difference is $\delta = 2\pi nd\cos\theta/\lambda$, substituting the value of δ and d, we get $\theta = 0$, that is normal incidence. The reflectance at normal incidence is given by

$$r = \left[\frac{n_{\text{air}}n_s - n^2}{n_{\text{air}}n_s + n^2}\right]^2$$

Where, n_s = refractive index of the substrate
n_{air} = refractive index of air
n = refractive index of the film

As the objective is to achieve zero reflectance, R is set to zero and the refractive index of the film (n) is found to be $\sqrt{n_{\text{air}}n_s}$. The fact that reflectance (R) proposed by Fresnel is dependent on the s and p-polarization of the light, the anti-reflective property is also analyzed on the basis of those parameters, as we will subsequently see.

The above analysis was done on the basis of a single layer on the substrate. For multi layered ARC the basic principle remains the same; the only difference lies in the mathematical model which relies on vector analysis of the individual reflected rays. The reflected light from the interface ij between the adjacent layers i and j is given by[5]

$$R_{ij} = |R_{ij}|\exp[-2(\delta_i + \delta_j)]$$

Where, $|R_{mn}| = [(n_i - n_j)/(n_i + n_j)]$ and phase thickness of each layer is given by $\delta_i = 2\pi n_i\cos\theta_i d_i/\lambda$ (θ_i is the angle of refraction, d_i is the physical thickness of the layer and λ is the wavelength of light. As shown in Fig. 1 (b) the reflection vectors originate from each of the ij interface, the resultant reflection vector can be expressed as

$$R_{\text{sum}} = R_{01} + R_{12} + R_{23} + R_{34} + R_{4s}$$

where $R_{01} = |R_{01}|$

$$R_{12} = |R_{12}|\exp[-2(\delta_1)]$$

$$R_{23}=|R_{23}|\exp[-2(\delta_1 + \delta_2)]]$$

$$R_{34} = |R_{34}|\exp[-2(\delta_1 + \delta_2 + \delta_3)]$$

$$R_{4s} = |R_{4s}|\exp[-2(\delta_1 + \delta_2 + \delta_3 + \delta_4)]$$

By minimizing R_{sum}, that is, by adjusting RI and film thickness of each layer, a state of anti-reflection can be attained.

3. Strategies to achieving anti-reflection

Anti-reflection can be imparted to a medium in two ways as demonstrated by researchers over the years. The basic model has

been imported from natural species such as moths[6,7] and it has been improvised by a host of computational findings and models to evolve into newer strategies.

3.1. Porous/patterned

In the previous section we determined the refractive index of a single film for zero reflectance and the value was $\sqrt{n_{air}n_s}$. However, the refractive index of the film can be lowered still by imparting porosity to it. Porous/density graded silicon (PSi) is the most widely explored material in this context.[8,9] Here the refractive index is dependent on the volume fraction because porous silicon (PSi) is a sponge like material marked with nanovoids. The refractive index can be lowered by lowering the fraction, f of Si, thereby increasing the proportion (1-f) of air.

Emulating best strategies of nature has been a worldwide research priority off late and this has led to the evolution of a whole new branch of science – biomimetics. In fact, the very inspiration of ARCs also comes from the eye of the moth. In order to disguise predators, the "moth's eye" or the corneal lens has evolved into absolutely lustreless surface thus, preventing light to reflect off it.[6,7] Scanning electron microscopy (SEM) reveals the fine nanostructure patterns or sub-wavelength structures (SWS) as they have dimensions smaller than the wavelength of light[7] as shown in Fig. 2. It is these microscopic SWS that interact with the incident light in a different way than the macroscopic structures. Light incident on a macrostructure would normally undergo reflection and scattering after being absorbed partly (Fig. 3(a)). However, light interacts differently when it falls on structures that have dimensions less than its wavelength, essentially the SWSs. Light interacts with the rough surface wholly as the wavelength of light is higher than the dimension of the structure and as if the surface has a gradient RI (Fig. 3(b)), light rays tend to bend progressively (discussed later, Rayleigh effect). If the same dimensional constraints are applied to the spacing and depth between nanostructures in textured or grooved surface, light rays get trapped in the crevices resulting in multiple internal reflections (Fig. 3(c)). It is this phenomenon that results in maximum absorption of the incident radiation thus, reducing the reflection in the visible range to 0.1%.[10]

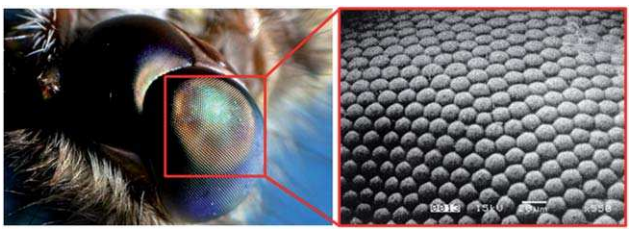

Fig. 2 The eye of the moth (left)[158] and the SEM image (right)[159] showing the nano bumps or protuberances on the outer surface of the corneal lens.

3.2. Gradient

An alternative way of reducing reflectance is to gradually reduce the refractive index of the film from the refractive index of the substrate (n_s) to the refractive index of air (n_{air}) (notice the variation in step and gradually in Fig. 4 (a) and (b) respectively). Gradient-index lenses are indeed naturally occurring and incorporate broad field vision in the eyes of antelope, aberration reduction in eyes of human and high spatial resolution in the eyes of eagles. In the area of anti reflectivity also this has a bearing to the effect that it imparts a smooth transition of refractive index from a higher value to the lower value of air.

The basic idea here comes from the seminal work by Lord Rayleigh[11] in 1880 on problem of gradual transition where he explained numerically that when density changes in a variable medium, reflection reduces and the ray bends as shown in Fig. 4 (c). These structures are called graded refractive index (GRIN) structures and the variation in refractive index follows several profiles (parabolic, cubic *etc.*) as we will subsequently see. The index matching or optical impedance matching as it is technically called is a crucial job as the adjustment of gradually reducing refractive index from substrate to the air is quite difficult. In fact, attainment of unity refractive index at the film-air interface is impossible. Therefore, the most practical approach in this field is to reduce the packing density of the films.[12] However, this affects the mechanical strength of the ARCs and thus, raises durability issues especially in outdoor solar panels.

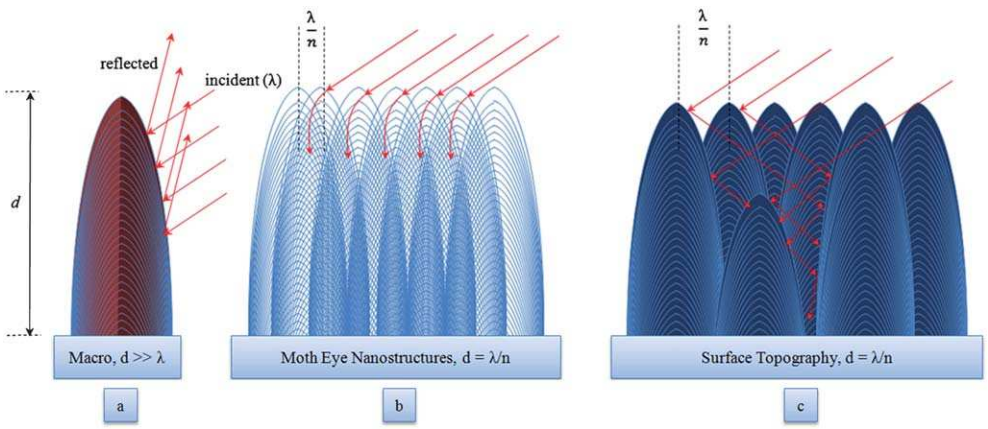

Fig. 3 (a) Light being reflected away from a macrostructure, (b) light interacting with the whole rough surface due to comparable dimensions, (c) light undergoing multiple internal reflections through a nanostructure pattern.

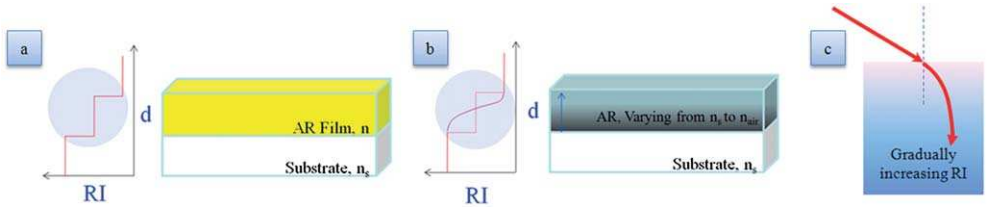

Fig. 4 (a) Sharp drop in refractive index observed in single layer anti-reflective films (b) smooth drop in refractive index from n_s to n_{air} in case of graded refractive index anti-reflective. (c) Light rays bending in the case of gradually varying RI medium.

4. Effective medium theory (EMT)

The digression at this point is very much in keeping with the fact that the EMT is an essential concept which is the cornerstone of many contemporary models and computational work in the area of anti-reflectivity. The basic idea to bear in mind is that materials with surface in-homogeneity (porous or a regular/irregularly patterned, rough surface or GRIN anti-reflective surface) have refractive index that depends on the topology because light gets scattered by nanoscale inclusions at times. Garnett[13,14] and Bruggeman[15] proposed the mathematical models to calculate the effective refractive index in this scenario (Table 1). Maxwell-Garnett (MG) proposed the technique to determine the "effective refractive index" of a "homogeneous" mixture under wave propagation. For a material mixture with volume fraction of inclusion f, MG model can be extended to give the effective refractive index as a function of f. Now if we have an inhomogeneous film the same can be considered to be consisting of layers of these "homogeneous" mixtures thus, determining the effective refractive index as a whole. A dichotomy can be established here between the MG model and Bruggeman's approximation. Consider a medium consisting of two media with refractive indexes n_1 and n_2 and volume fractions f_1 and f_2 ($= 1 - f_1$) respectively, the effective refractive index given by the two models is as reproduced in Table 1.

5. Requirements for perfect anti-reflectivity

5.1. Broadband anti-reflectivity

The anti-reflective property must be reasonably consistent over a broader spectrum of wavelength of the incident radiation. The fact that an optical impedance matching, in the visible region of the incident light doesn't ensure a match in the ultraviolet (UV) or the near infra-red (NIR) region, impairs the performance of some anti-reflective in the UV or NIR regions. In fact, normal incidence AR coating designs typically fail in spectral ranges $0.85 < \{\lambda_U/\lambda_L\} < 5$ where λ_L and λ_U are the lower and upper wavelengths, respectively.[16] In addition, we will also see subsequently how the behaviour of a single layer, double layer and multi layer anti-reflective affect the very property of reflectance minimization in different ways at times showing quite uneven suppression of reflectance as well.

Table 1 Maxwell's model *vs.* Bruggeman's model

Maxwell-Garnett model	Bruggeman approximation
Effective RI can be evaluated from the equation $\left[\frac{n^2-n_1^2}{n^2+2n_1^2}\right]^2 = (1-f_1)\left[\frac{n_2^2-n_1^2}{n_2^2+2n_1^2}\right]^2$	Effective RI can be calculated from the equation $f_1\left[\frac{n_1^2-n^2}{n_1^2+2n^2}\right]^2 + f_2\left[\frac{n_2^2-n^2}{n_2^2+2n^2}\right]^2 = 0$
This value is based on the assumption that the medium n_2 is surrounded by n_1. Thus, the equation will change if n_1 is surrounded by n_2.	This can be extended for k layers as $\sum_{i=1}^{k} f_i\left[\frac{n_1^2-n^2}{n_1^2+2n^2}\right]^2 = 0$

5.2. Omni-directional anti-reflectivity

It has been established by Fresnel that the angle of incidence plays a decisive role in the determination of reflectance. In fact, most glasses and plastics with RI around 1.5 show a 4% reflectance at normal incidence but a 100% reflectance at grazing angles. This same phenomenon is observed in anti-reflective films and numerous designs catering to incident angles from 30° to 60° from the normal have been proposed.[17,18] In fact, this poses a challenge in case of silicon photovoltaic which need to be mechanically oriented to face the sun throughout the day. This obviously requires a control mechanism which involves additional overheads and consumes energy. Omni-directional anti-reflectivity is one of the ways this issue can be addressed.

5.3. Polarization insensitivity

The effect of the two types, s and p polarization of light on the ARCs also needs analysis. The s-polarization has the electric field perpendicular to the incidence plane and p-polarization has the electric field parallel to the incidence plane. Polarization plays a very important role in antiglare coatings (AGCs) and ARCs due to the fact that light reflecting at shallow angles has the p-polarized light reflecting to the maximum and sunlight indeed shows appreciable degree of polarization.

6. Types of anti-reflective coatings (ARCs)

6.1. Type I (based on the layer composition)

6.1.1. Homogeneous ARCs. A single homogeneous layer of refractive index n, will impose restriction on the RI and thickness that we have already discussed. The RI must obey $n = \sqrt{n_{air}n_s}$ and thickness equal to $\lambda/4$. However, if the substrate is surrounded by air, n_{air} is unity and n largely depends on n_s. Thus, as discussed earlier, a porous or pattern layer lowers the n considerably thereby facilitating optical impedance matching (Fig. 5 (b)). Moreover, multiple thin layers in a homogeneous set

up also help achieve zero reflectance at certain wavelength(s) though the RI rule is not strictly obeyed.

6.1.2. Inhomogeneous ARCs. Inhomogeneous ARCs follow the gradient RI approach to achieving anti-reflectivity. For a quick recall, the contribution to reflection from abrupt interfaces is progressively reduced with depth due to varying RI from n_{air} to n_s. The overall thickness of the layer in this case is not critical[19] from the design point of view though it's better to have thickness more than λ_U or $2\lambda_U$, where λ_U is the upper wavelength of the incident light.[21] The inhomogeneous ARCs can be approximated to a large number of sub-layers where RI difference between adjacent sub layers is very small (Fig. 5 (f)). If we consider $n_{air} = 1$, the inhomogeneous layer can achieve zero reflectance provided the layer thickness follows the aforementioned λ_U limit and the layer is incorporated with SWS as shown in Fig. 5(f). The EMT discussed earlier can indeed help evaluate the RI in this case.

6.2. Type I (based on the layer composition)

6.2.1. Single layer ARCs. These are used for moderate suppression of reflectance to 2.5% for a very broad spectral range, like 450–1100 nm at normal incidence.[159] However, the selection of material is a challenge because the RI of glass is 1.5151 (BK7 at 633nm) and calculations would set RI to approximately 1.22. Single layer magnesium fluoride (MgF_2) is the most commonly used ARCs under this type because its RI is 1.38 and it reduces surface reflectance of BK7 glass from approximately 4% to less than 1.3% at the specified centre wavelength and normal incidence.[160] Even though the performance of single layer MgF_2 ARCs is not exceptional, the advantage is its broad usable wavelength zone as can be seen in Fig. 6(a).

6.2.2. Double layer ARCs. In order to reduce the reflectance further still, the double layer ARCs can be employed. The necessary and sufficient index condition for a double-layer coating with equal optical thickness ($n_1d_1 = n_2d_2 = \lambda/4$) to give zero reflectance is:[22]

$$\frac{n_1}{n_2} = \sqrt{\frac{n_0}{n_s}} \quad \text{or} \quad n_1 n_2 = n_0 n_s$$

The first equation produces one minimum (Fig. 7(a)) where reflectance becomes zero and the second equation has two minima and one weak central maximum. These double layer coatings are called v-coatings due to the V-shape of their profile and quarter–quarter coatings also due to their thickness relationship. These V-coatings are the perfect solution for especially laser applications, where resistance to intensive laser radiation is important and minimum reflection is required only at a specific wavelength.[161]

The discussion above was considering glass as the reflecting surface. However, since the outdoor solar panels suffer from two tier reflection one at the protective glass and the other on the Si PV surface we would also take a glance at a research undertaken by using single layer thin films of SiO (RI 1.85), CeO_2 (RI 2.2) and ZnS (RI 2.3) on Si substrate and subsequently for

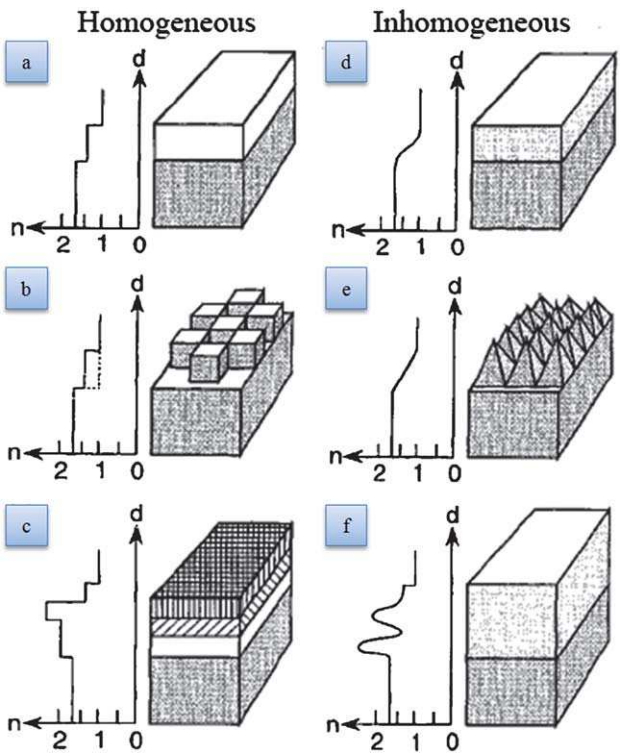

Fig. 5 Homogeneous ARCs, single layer (a), patterned (b) and multi-layer (c) and inhomogeneous ARCs, single layer (d), patterned (e) and multi-layer (f). Notice the variation in refractive index with respect to film thickness.[19]

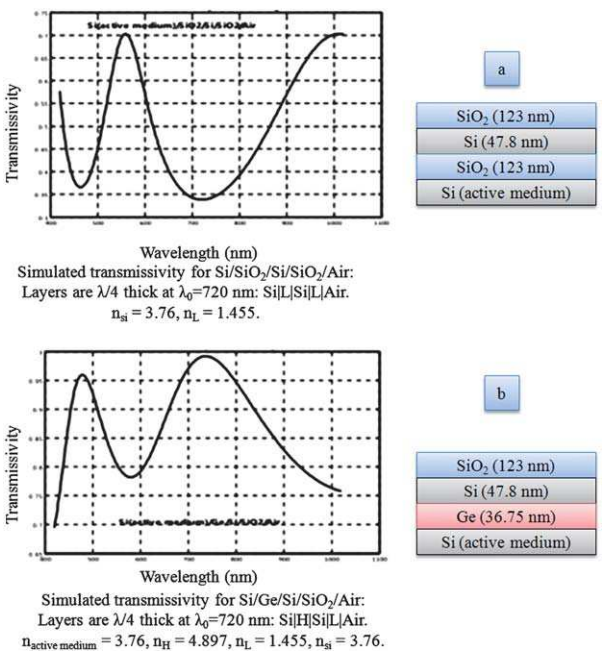

Fig. 6 Simulated transmissivity of (a) Si(RI 3.76)|SiO2(RI 1.455)|Si|SiO2|Air, $\lambda/4$ thick layers, (b) Si (RI 3.76)|Ge (RI 4.897)|Si|SiO2(RI 1.455)|Air, $\lambda/4$ thick layers multi layer ARCs.[20] *NB. Caption in the figure has been enhanced for clarity.*

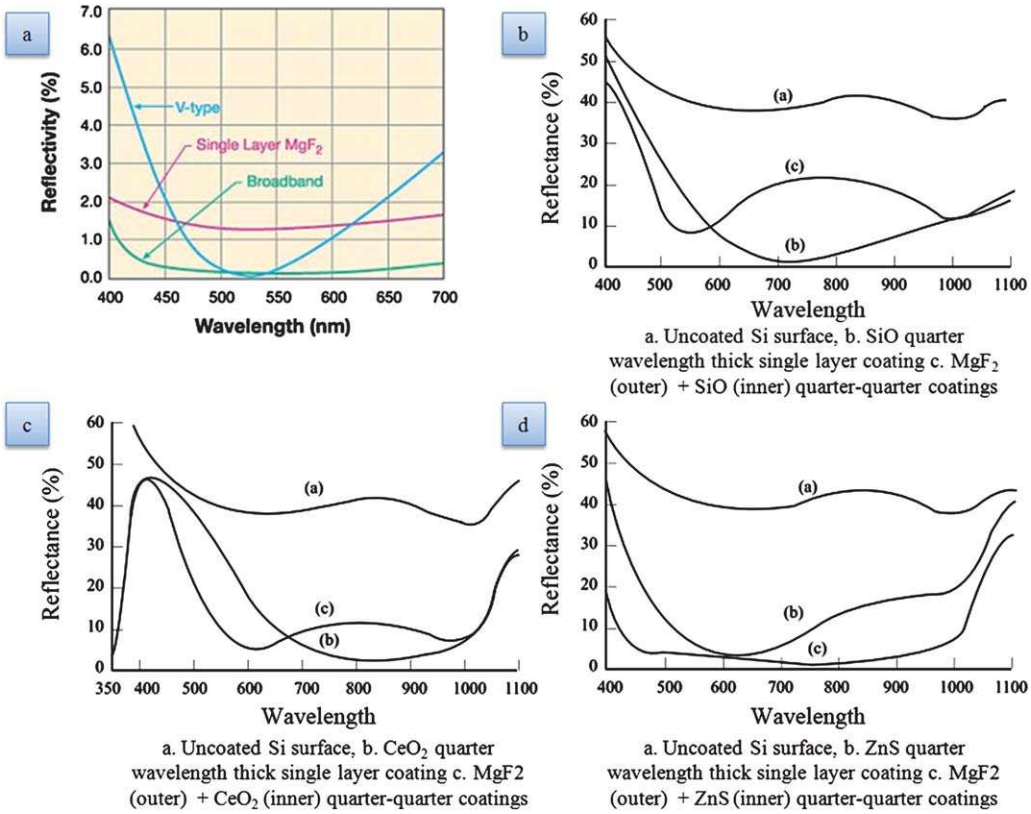

Fig. 7 (a) Comparative study of reflectivity *vs* wavelength of the single layer MgF_2, V and broadband coatings[161] (b, c, d) Comparative study of uncoated Si surface, single layer AR ($SiO/CeO_2/ZnS$) and double layer (MgF_2 {outer} + $SiO/CeO_2/ZnS$ {inner}) coatings.[23]

V-coatings, MgF_2 (RI 1.38) as outer layer and SiO ($n_2 = 1.85$), CeO_2 ($n_2 = 2.2$) and ZnS ($n_2 = 2.3$) as an inner layer on silicon (RI 3.5 $\sim$ 4 at 400 $\sim$ 1100 nm).[23] The results indicate a phenomenal drop of reflectance from 56.8–37.5% (spectral range 400–100 nm) for uncoated Si surface to below 5% by using single layer ARCs made of $SiO/CeO_2/ZnS$. The double-layer quarter-quarter coatings also offer interesting results. MgF_2 (outer) + SiO (inner) have two reflectance minima at 540 nm (reflectance 8.9%) and 1021 nm (reflectance 12.6%) separated by one marginal maxima at 802 nm (reflectance 22.7%) (Fig. 7(b)). However, when we consider MgF_2 (outer) + CeO_2 (inner) the minima are observed at 601 nm (reflectance 4.9%) and 997 nm (reflectance 6.9%) respectively, thus making this a better choice over the MgF_2 + SiO. At last, MgF_2 (outer) + ZnS (inner) registers a drop in reflectance from 20% at 400 nm to 0.9% at 720 nm and a quick relook at Fig. 7 (b), (c), (d) would make it quite obvious that MgF_2 + ZnS has a wider profile than the others, thus complying to broadband.

6.2.3. Multi layer ARCs. As we are gradually drifting towards broadband anti-reflection (BAR), the multi layer ARCs come into the reckoning. However, the trade-off between a larger bandwidth and overall reflectivity is the challenge facing us. The mathematical analysis of multi layer ARCs is just an extension of the earlier destructive interference type vector model we had discussed.

The mathematical model for the multilayer coatings has been discussed in section 2 and just to recollect, the summation of all the reflected vectors must be minimized by adjusting the RI and the thickness of the film. A computational study[20] in this area analyses the transmissivity curves in the far red zone (720 $\sim$ 750 nm) as shown in Fig. 6 of multi layers on Si substrate. The results reveal that the insertion of an extra layer of Si between the high index Ge and the low index SiO_2 has maximum blue transitivity of approximately 96% (at 480 nm). Similarly, in many biological species such as Coleoptera, alternate high and low RI layers facilitate optical interference.

6.2.4. Gradient refractive index ARCs. As already discussed, gradient RI coatings have their RI profile following different curves such as linear, parabolic, cubic, quintic, exponential, exponential-sinusoid *etc.* and comply with the Rayleigh effect. Southwell has proposed in his study of gradient ARCs,[24] equations governing various gradient refractive index (GRIN) profiles which are given below (RI of incident medium (*e.g.*, air) is n_i and RI of substrate is n_s):

Linear index profile, $n = n_i + (n_s - n_i)\, t,\ 0 \le t \le 1$

Cubic index profile, $n = n_i + (n_s - n_i)\, (3t^2 - 2t^3)$

Quintic index profile, $n = n_i + (n_s - n_i)\, t\, (10t^3 - 15t^4 + 6t^5)$

Similarly, Sheldon and Haggerty have proposed some interesting results[25] on GRIN profiles involving linear, concave and convex-parabolic and cubic curves under transverse electric (s-polarized) waves. Notice the oscillation in percentage reflectivity *vs* (d/λ) curve in Fig. 8(a) which turns out to have the same period and varies with the angle of incidence. In 2007, Xi *et al.* have also demonstrated a GRIN profile made of 450 inclined SiO_2

nanorods that gives an overall RI of 1.05[26] and they propose a quintic profile to be the best AR profile (Fig. 8(b)). Moreover, three layers of TiO_2 nanorods and two layers of SiO_2 nanorods above it, all having quintic profiles render a hybrid system of multi-layer quintic RI coatings and it registers a RI of 2.03 for the bottom layer and RI of 1.05 for the top layer and a reflectivity of as low as 0.1%. In fact, something similar has also been studied by Dobrowolski *et al.*[19] computationally where the GRIN profile is likened to a 200 layers simulated ARCs where the RIs of adjacent layers differ by 0.01. The average reflectance has been computed to be less than 0.05 and 0.01 for all angles less than 85° and spectral region 5.0–8.0μm, respectively, and the comparison with a 4-layer system is also shown in Fig. 8 (c), (d). However, the findings of Schubert *et al.*,[27] 2010 runs contrary to the popular notion of GRIN outdoing multi layer ARCs in all ways.

The underperformance of GRIN is attributed to two factors (i) there is a gap in the RI between the upper surface of GRIN ARCs (minimum attainable 1.05) and ambient air (unity RI) and (ii) at the coating-substrate interface, because the absorbing substrate has a complex RI and transparent ARC has a real RI, a mismatch exists. It is this discrepancy that violates the Rayleigh effect and the fact that a multi layer ARCs basically facilitates destructive interference type anti-reflection, the results are quite explicable in Fig. 8(e).

6.3. Type III (based on the surface topography)

The development of this type was essentially triggered by the requirement of omnidirectional AR property while retaining broadband AR as well.

6.3.1. Porous ARCs. A great deal of research has been undertaken in this area[8,28–30,130,131] especially relating to porous silicon (PSi) because of its application in the field of solar energy harvesting. PSi consists of nanometre-sized voids with a large hydrogenated surface.[30] The relationship between refractive index and porosity is proposed differently in different studies; for example,

$$n_{pc} = \left[\left(1 - \frac{P}{100}\right)(n_{dc}{}^2 - 1) + 1\right]^{\frac{1}{2}}$$

where n_{pc}, n_{dc} and P are the RI of the porous and dense media and the porosity percentage respectively.[31] However, EMT is the computational foundation for all RI calculations. The porosity and consequently, reflectance depend on the solution composition, porous film growth rate[32] and film thickness. Reflective properties of PSi films on the outer region of p/n^+ junction have been studied with regards to solar cells[8] by etching the outermost region in the presence of HF/HNO_3. The study claims that a 1500 Å thick layer gives the best photovoltaic conversion efficiency (12%) for 10 × 10 cm^2 multicrystalline devices. A comparative study (Fig. 9(c)) involving PSi and other textured surfaces, exemplifies PSi as the most effective medium to reduce scattering. Complying results were also obtained (Fig. 9(a),(b)) in case of tetraethyl orthosilicate (TEOS) + ethanol (EtOH) porous layers with the transmittance pegged at 99.6% (AR-1) and 99.4% (AR-2) and reflectance varying between 0.15–0.8%.[33] In addition, low reflection silica films have also been reported to have a low reflectance of 0.2% while being chemically inert, abrasion resistant and durable.[28]

A discussion on the manufacturing process would involve state-of-the-art techniques not discussed thus far which is why only a brief outline, in the context of porous films, would be presented here. Glass used phase separation and etching[4,7,34] were the formative technology for fabrication of porous layers. In recent times, sol–gel,[35] adsorption of colloids into polyelectrolyte multilayer[36] and selective dissolution of spin-coated films[37,38] have been adopted for fabrication of a nanoporous film.

6.3.2. Biomimetic photonic nanostructures ("moth's eye"). Nature has perfected the optical systems so well that it indeed makes perfect scientific sense to imitate them and if examples are to go by, scallop eyes inspired chromatic aberration minimization, horsefly cornea inspired extreme UV-optics and human deformable eye lenses inspired liquid lenses still strive to attain the perfection nature has achieved.

The camouflaging strategy of some insects and the exceptional photon collection capability of nocturnal creatures enabling them to see at night motivated scientists to analyze the eyes of such night-active insects, especially moths (Fig. 10(a)) and butterflies[39,40] and transparent wings of hawkmoths.[41] It turned out that the corneal surface in the eyes of moths has a hexagonal array of sub wavelength (SW) conical or cylindrical nanostructures known as nipple-array. The diameter of each of these protuberances is found to be 100 nm and are 170 nm away from one another[42] (Fig. 11(b)).

Not just broadband and omnidirectional AR, these nanostructures are found to remove disparity in the reflection for polarized lights as well though research now shows that butterfly eyes are highly sensitive to polarized light.[43] Further investigation revealed that these nanostructures have a gradient RI between chitin (polysaccharide RI 1.54, consider substrate) and ambient (RI 1.0)[44] which makes it clear that AR is primarily due to exceptional transmission (Rayleigh effect). The first reproduction of "moth's eye" structure involved crossing of three gratings at 120° using "lithography".[45]

Precision and scalability (onto lenses and solid plastics) requirements led to the fabrication of highly accurate "moth's eye" structures using electron-beam etching. A very interesting finding by Boden *et al.*[46] which involves the study of anti-reflectivity throughout the day shows computationally that moth's eye arrays of 250 nm show similar performance as the double layer ARCs we have already discussed. However, an increase of height to 500 nm reduces the reflection losses by 25% thus, translating the extra photon collection to 12% rise in energy of a solar cell. Rigorous probe of eyes of other species revealed sinusoidal gratings (RI = $f[\sin g(x)]$) of 250 nm periodicity in the cornea of amber[47] (Fig. 11(a)) which has outstanding broadband properties.

Several other profiles in the domain of "moth's eye nipple array" have also been analyzed,[48,49] namely, conical, paraboloidal (Fig. 11(d)) and Gaussian-bell shape and it has been reported that paraboloidal nipple array displays best performance among these (Fig. 11(b),(c)). Thus, it has been proposed that tall paraboloids with base touching each other at hemispherical facet surface results in the best reduction of reflectance.[48] The rigorous study of corneal samples of 361 species by Bernhard *et al.*[49] has been a landmark contribution in this area.

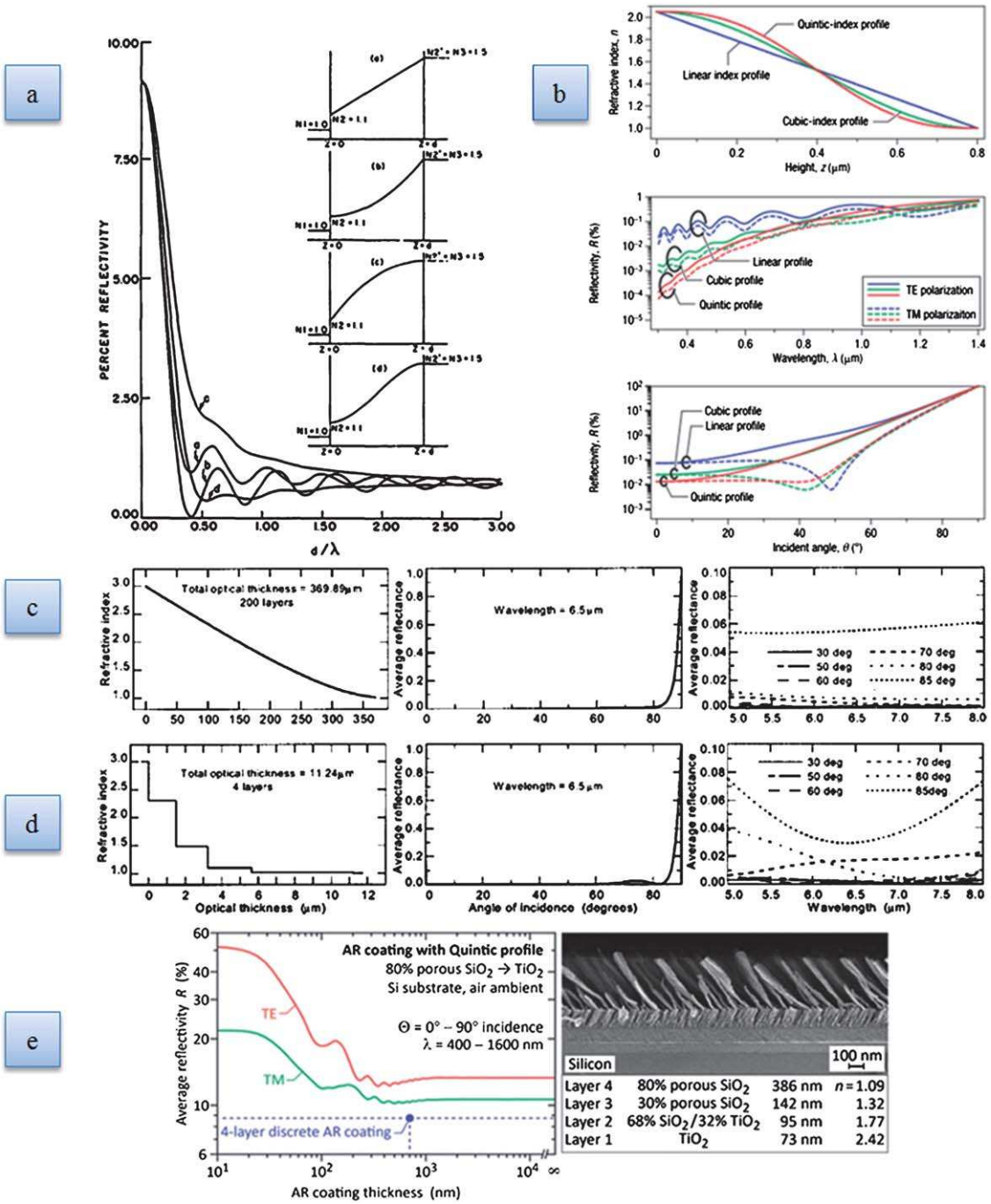

Fig. 8 (a) Reflectance of s-polarized waves at 450 incidences for semi-bound a. linear b. concave-parabolic c. convex-parabolic d. cubic profile. Semibound- notice the difference in N1 and N2,[25] (b) a. Linear, cubic and qunitic index profile (ns = 2.05) showing RI *vs* height or thickness, reflectivity *vs* wavelength and reflectivity *vs* incidence angle. Notice the superior performance of qunitic profile (lowest R),[26] (c) Simulated 200 layer AR coating and (d) simulated 4 layer AR coating to analyze the GRIN effect through multi-layer approximation,[19] (e) (left) reflectivity *vs* angle and wavelength of ARC with quintic profile and 4-layer ARC of thickness 400 nm under transverse electric (s-polarized) and transverse magnetic (p-polarized) flux. Notice the 13.59% reflectivity of quintic compared to 8.86% for 4-layer under p-polarized light and 10.76% reflectivity of quintic as opposed to 8.60% for 4-layer under s-polarized light. (right) SEM image showing composition and arrangement of the four layers on Si substrate.[27]

We have seen the height (< λ/2), inter-nipple spacing and shape in "moth's eye" structures playing a pivotal role than the width of the "moth's eye" (Fig. 11(c)).

The idea has been extended onto quartz[50] and fused silica substrate with conical array reducing reflectance to 0.5% in 400–800 nm,[51] polymer[7] and GaSb[52] and many other materials.

Moreover, SWS have been found to have excellent compatibility with the substrate material compared to multi-layer thin films discussed earlier. The latter reportedly has adhesion issues due to thermal coefficient difference between the substrate and the adjoining layer or between adjacent layers which predominantly gives rise to "debonding" problems. It is worth

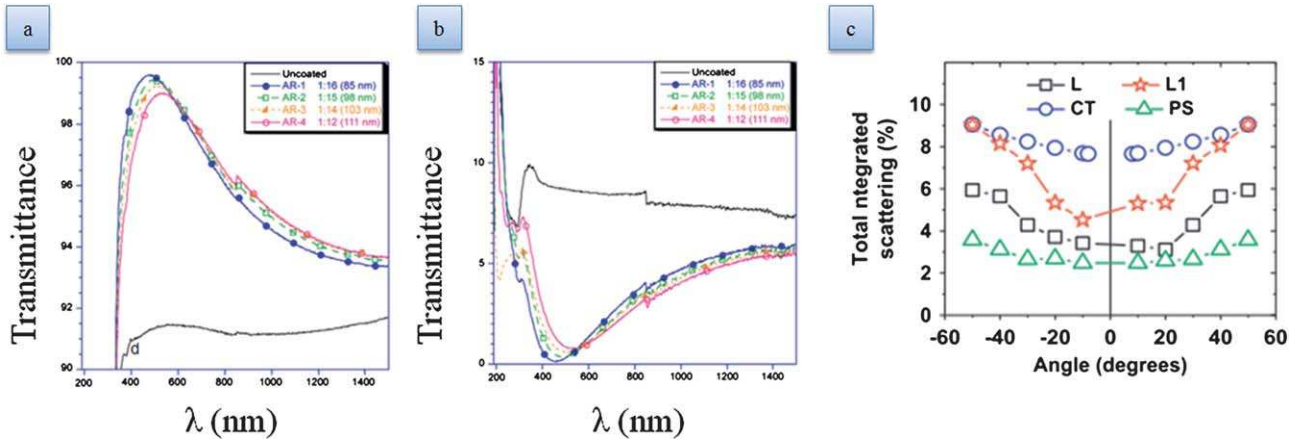

Fig. 9 (a) Transmittance, (b) reflectance of uncoated glass and coated AR samples. AR-1, AR-4 *etc.* show the ratio of TEOS:EtOH and film thickness.[33] (c) TIS *vs* angle for $\lambda = 980$ nm comparing ultrafast laser textured Si {L}, annealed ultrafast laser textured Si{L1}, chemically textured Si with SiNx {CT}, Porous Si{P}.[72]

mentioning the preference of some researchers[53] for rigorous coupled wave analysis or RCWA (solutions to Maxwell equations) over EMT as the former predicts the dimensions of the crucial parameters more effectively thus, offering better ways of optimization.

6.3.3. Textured surface ARCs. Surface texturing also renders the substrate anti-reflective as demonstrated by many scientists since 1960s[54] and the reason for AR is the phenomenon of light trapping and multiple internal reflections.[55,56,132,133] In an effort to produce high efficiency solar cells with no ARCs, Smith *et al.*[57] report a new texturing geometry as shown in Fig. 12(b) (mechanism of light bouncing shown in Fig. 12(c)) which outperforms the perpendicular slats geometry for texturing proposed by Landis (1987) (Fig. 12(a)). This texture geometry has three perpendicular planes (3PP) that facilitate multiple internal reflections due to planes arranged in a way to make the incident angle greater than the critical angle (Fig. 12(b)) which is how the 3PP geometry keeps the largest percentage of rays in optical confinement (15 bounces). Lambertian texture on the rear surface of the solar cell also produces the same light trapping effect but when used with pyramid (Fig. 12 (f))[58] or inverted pyramid textures[59,60] on the top surface, it shows performance comparable to or better than 3PP). Note that the spacing of the structures and depth of the same is an important tunable factor. Surface texturing imparts a reduction of reflectance by approximately 10%[61] in mono-crystal Si and reflection losses are reportedly minimized to nearly 1% in case of amorphous Si[62] using surface texture.

A few other interesting surface texturing or light trapping structures have been reported such as honeycomb-textured structures[63] that reduce reflectance to 10% around 600 nm and light trapping 2-μm silica microsphere coatings (Fig. 12 (d))[64] on glass substrate that reduce reflectance (7.6%) and increase transmittance (92.7%) around 400 nm (up to 1100 nm). Fig. 12 (e) pictorially explains the underlying concept. In fact, a honeycomb textured surface[60] has reportedly enhanced the efficiency of multicrystalline and monocrystaline solar cells by 19.8 and 24.4%, respectively, against the author's claim of the highest reported lab statistics of 18.6 and 24%, respectively.

Rayleigh effect is also perceived in case of surface texturing besides the dominant multiple internal reflections. A study by Craighead *et al.*[10] shows that by making cross sectional dimensions substantially smaller than λ, spatial variation (linear) in RI can be attained and the same has been employed in reflectance reduction in several cases.[10,62]

6.3.4. Anti-reflection grating (ARG). Broadband antireflection requirement over a large region even up to the terahertz (0.1 ~ 10 THz, 30 μm to 3 mm wavelength[65]) range gets fulfilled by the surface relief gratings or ARGs. The grating structures work on the same principle of creating a continuous gradient of RI (n_s to ambient, 1) and their efficacy has been proved in the solar,[66] microwave[67] and THz[68] wavelength ranges. However,

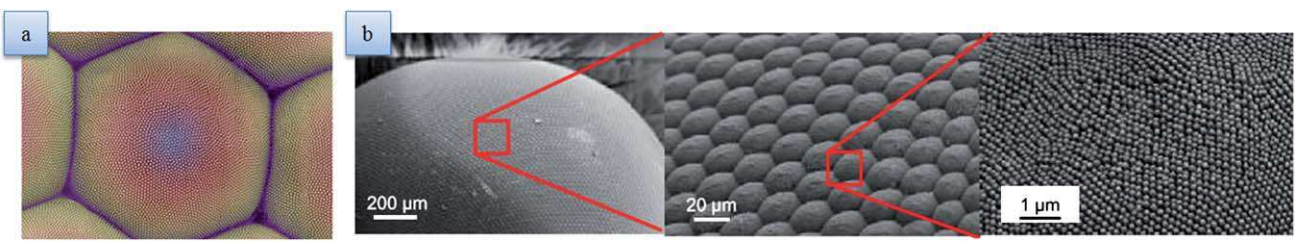

Fig. 10 (a) SEM image showing tiny bumps on moth's eye,[162] (b) highly magnified drill down SEM images showing the hexagonal array of SW nano structures.[42]

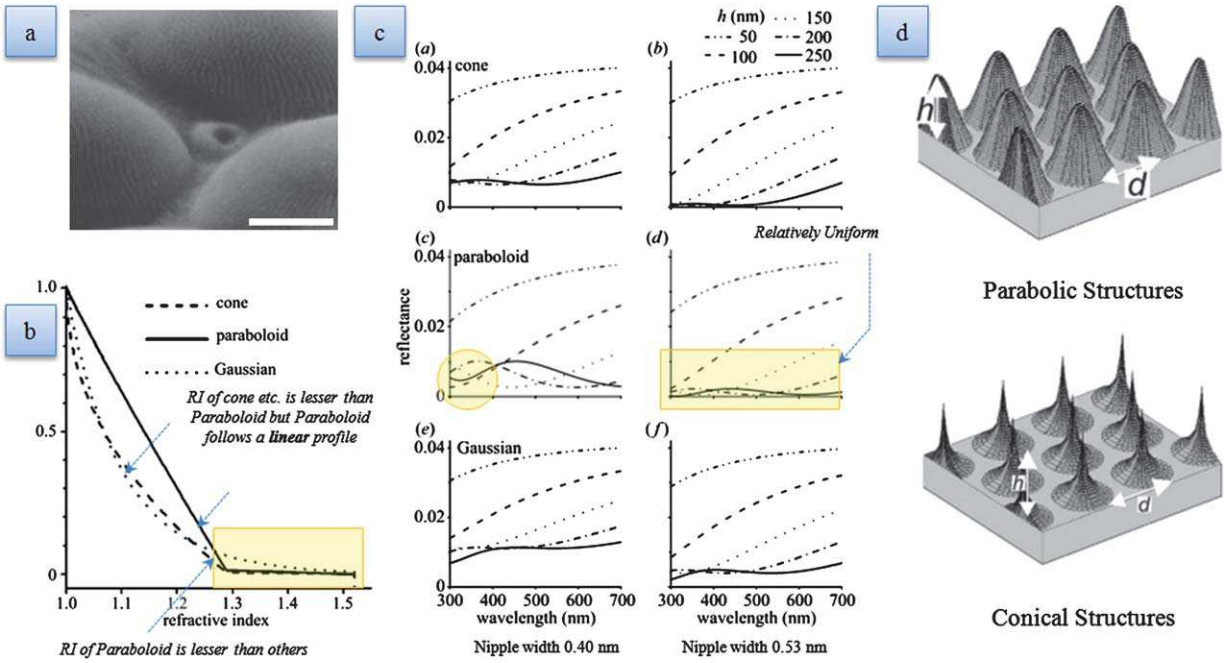

Fig. 11 (a) Sinusoidal gratings on the cornea of amber;[47] (b) variation of RI w.r.t height for three different nipple arrays; (c) reflectance *vs* wavelength for the three arrays.[48] Notice the linearity and lowest reflectance for a parabolic shape. (d) Computer simulations of moth's eye.[53] *NB: Fig. 11 (b) & (c) have been highlighted and illustrated for better understanding.*

ARGs have been found to be less effective in case of solar cells because gratings basically help propagate the zeroth diffraction orders (directly transmitted and reflected light) and don't cater to higher diffraction orders which apparently contribute to the total energy collected in a solar cell. Computational results from a study by Brückner *et al.*[68] show that a one dimensional ARG with a triangular cross section and spacing of 50 μm and depth of 100 μm, produces a transmittance of over 99% (Fig. 13(a)) in the 0.75 to 3 THz range and if the same cross section with revised dimensions, period = 0.5 mm and depth = 1 mm is subjected to the flux, 0.1 ~ 0.4 THz, shows 99.5% transmission but beyond 0.4 THz, transmission reduces drastically (Fig. 13(b)). However, there is a way to avoid the diffraction grating. The period p of the gated structure should follow the relationship $p < \lambda/n_s$.[69] In this scenario, an array of square base pyramids have been reported[70] to be optimum as the RI of the grated system can be

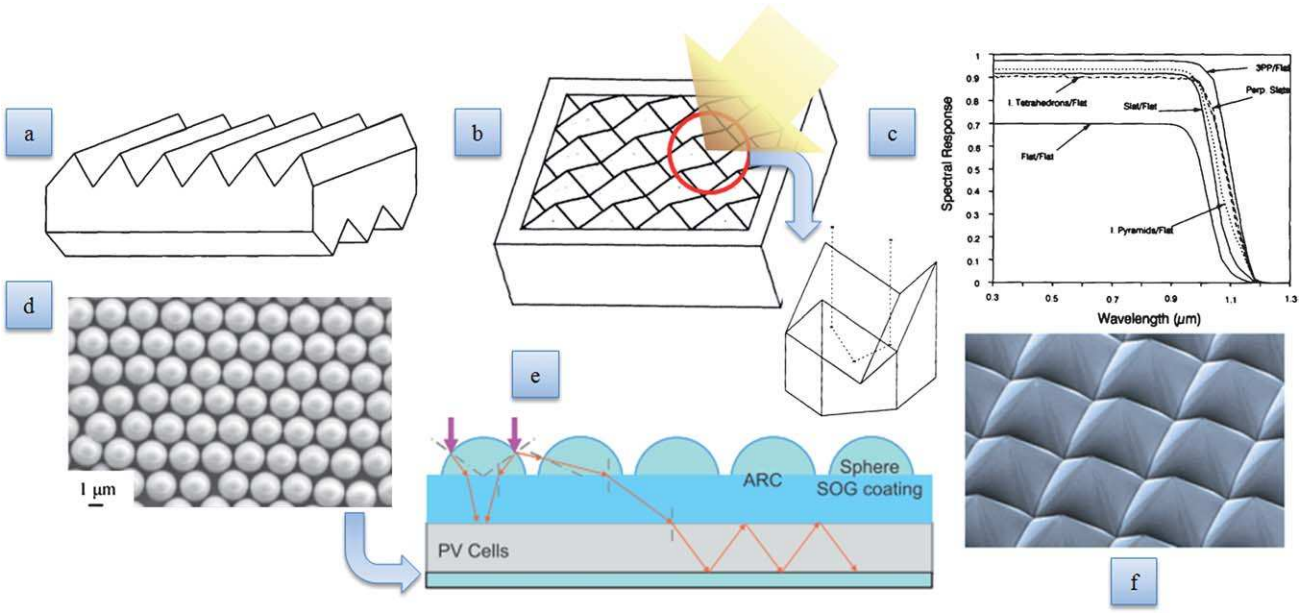

Fig. 12 (a) Perpendicular slat geometry for textured solar cells;[57] (b) 3PP geometry for textured solar cells displaying the multiple light bounce effect;[57] (c) mechanism of light bouncing off the 3PP geometry;[57] (d) SEM image of 2-μm silica microsphere on glass;[64] (e) multiple internal reflection through the AR coating comprising the silica microsphere;[64] (f) pyramid texture on Si surface (apex angle 720, base length 110–30 μm).[58]

approximated to a quintic profile [$n_i + (n_s - n_i)\, f(\text{thickness}^5)$] that has already been proved effective in ARCs. Fig. 13(c) shows the grated surface relief pattern on a substrate with RI 1.45.

Another such sub wavelength pyramid shaped surface relief grating comprising a stack of eight binary layers[71] has been imparted to multi-crystalline Si widely used in solar cell applications. It is reported that for a 100 nm depth and aspect ratio (depth/periodicity) of 100 nm reflectivity scales up at less than 1% in the visible range (Fig. 13(d)). Fabrication techniques such as laser-interference lithography and nano-imprinting which are used to produce the ARGs will be dealt with in the next section.

7. Fabrication techniques of anti-reflective coatings (ARCs)

Most of the ARCs being nanostructure based can have their fabrication techniques classified under the same broad subtractive top-down or additive bottom-up techniques of nanotechnology. There are indeed a few other unconventional techniques which will be brought under the spotlight.

7.1. Conventional fabrication: bottom-up technology

7.1.1. Sol–gel processing. This is one of the most prevalent technologies for the production of porous ARCs. This process involves the use of inorganic salts or metal alkoxides as precursor materials which when exposed to aqueous or organic solvent, hydrolyses and condenses to form inorganic polymer comprising metal-oxide-metal bond.[73] The different coating techniques adopted to coat sol-gels will be discussed in brief here.

Illustration 1 Fabrication techniques for ARCs discussed

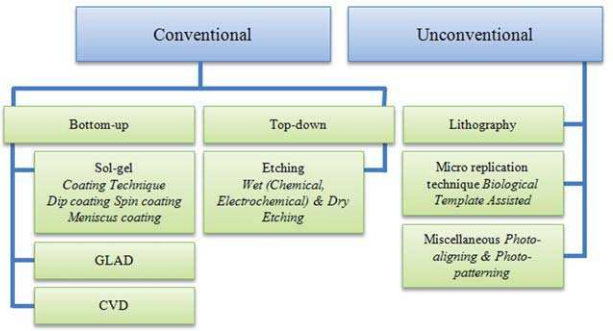

Dip coating. In this process the substrate is dipped and withdrawn from the desired solution at a controlled rate (feed velocity). The stages in the process can be enumerated as immersion, start-up, deposition, evaporation and drainage (steps in Fig. 14(a)).

Spin coating. It is a batch-production technique which produces thin films on flat or marginally curved substrates. It involves deposition of a small puddle of viscous film material and subsequent spinning of the substrate at high angular speed (*e.g.*, 3000 rpm) thereby forcing the puddle to spread owing to centripetal force (steps in Fig. 14(b)).

Meniscus coating. This technique involves flowing of coating material through porous applicator onto the surface of the substrate. The crux of the technique is to maintain menisci of the

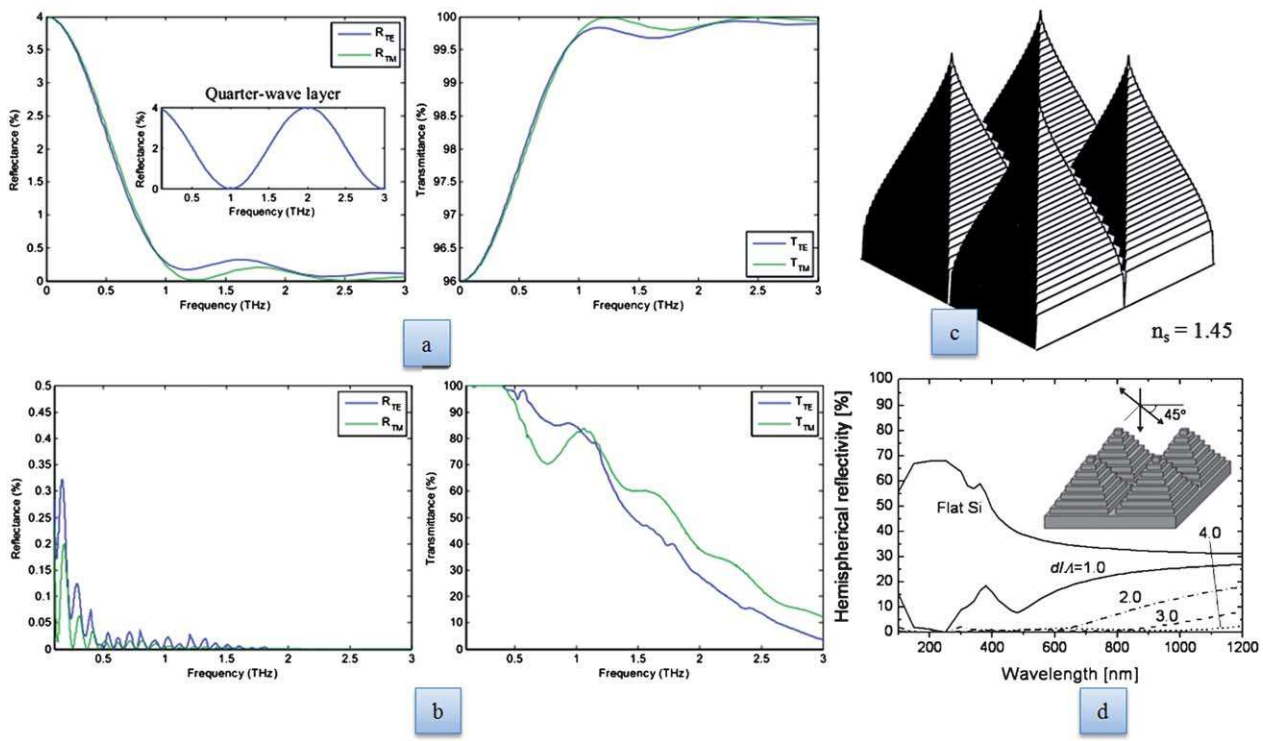

Fig. 13 Reflectance and transmittance for triangular ARG of (a) period 50 μm and depth 100 μm (b) period 0.5 mm and depth 1 mm.[68] (Results of rigorous coupled wave analysis) (c) optimum ARG profile for substrate RI 1.45[70] (d) grated pyramidal structures on multi crystalline Si (Λ = periodicity, 100 nm, d = thickness of the grating) & reflectivity *vs* wavelength for d/Λ.[71]

coating material between the applicator and the substrate which can produce micron thick films on the substrate. This technique is used in flat panel displays, optical devices and Si, Ge wafers *etc.* An enhancement of this used in paint industry is demonstrated in Fig. 14(c).

Since 1964[134] sol–gel process has been industrially used to produce ARCs. Production of porous ARCs is an area where sol–gel is extensively used and studies show that the desired minimum pore-size and maximum pore-volume is achieved by varying the mixing ratio in the mixture of two insoluble materials judiciously and subsequently dissolving one of them using a solvent thereby rendering the other material porous.[37]

For instance, a mixing of polystyrene and polymethyl-methacrylate (PMMA) in the solvent tetra-hydrofuran (THF), followed by spin-coating on a transparent substrate and subsequent treatment with cyclohexane that dissolves polystyrene is a way of producing a porous PMMA film.[37] This film has RI varying between 1.225 and 1.285 and transmittance 99.7% in 400–680 nm range. Interference type ARCs comprising TiO_2/SiO_2-TiO_2-SiO_2 (3 layer) on glass[74,75] used in contrast enhancement filters for monitors, SiO_2 coatings deposited on low emissivity glazing (windows) by dip-coating resulting in 10% increase in transmittance in visible region, colloidal solution being explored as precursor material for porous coatings[76] and use of the same in high power optics,[135,136] sol–gel processed ARCs for cathode tubes (CRTs),[77,137] Al_2O_3 porous low index layers for CRT faceplates and solar collectors[138] are quite a few examples indicative of the versatility of the sol–gel technique. A cursory look at the developments in the field of solar cells with regards to sol–gel technique again provides us with a wealth of information. Sprayable TiO_2 ARCs for solar cells in 1980,[139] two-layer interference ARCs (layer 1: TiO_2 RI 2.4, layer 2: 10%TiO_2, 90% SiO_2 RI 1.4) for photovoltaic resulting in a rise in conversion efficiency by 49%,[140] bi-layer multi functional nanostructure material incorporating anti-reflectivity, hydrophobicity, antifogging properties *via* sol–gel method[78] just goes to shows the continued interest in sol–gel processing of ARCs.

On the flip side, however, sol–gel prepared films at times have un-reacted or un-removed solvent materials that might influence the properties of AR. In addition, controlling the thickness of the film apparently is the trickiest part.

7.1.2. Glancing angle deposition. This is basically a physical vapour deposition technique involving condensation of vaporized material onto a substrate. An improvement to this technique is the glancing angle deposition (GLAD) that has the vapour flux incident at an angle on a rotating substrate. The advantage in so doing is that the thin film grows with a gradually decreasing density there by, increasing porosity due to "atomic-shadowing" (Fig. 15(a)) and this technique also gives high degree of control over the morphology of the resultant nanostructure. However, it is obvious that the angle of material deposition/growth, in turn, porosity of the film is dependent on the angle of vapour incidence.[79] A relationship between the oblique angle α and column angle β is give by Tait *et al.*[80] as $\beta = \alpha - k \sin[1 - \cos \alpha/2]$. Thus, if the material is deposited at large oblique angles the porosity of the film will increase and *vice-versa*. In order to counteract this, an enhancement was proposed by K. Robbie[79] which impart two substrate motions, rotational about the axis perpendicular to the substrate as discussed and secondly, rotational about an axis shown in Fig. 15(b).

Based on the sculptured thin film (STF) deposition,[81] GLAD technique has been modified in different ways to engineer films with slanted, chevron, helix, vertical and other morphology based nanostructures (Fig. 15(c)–(f)). GLAD assisted ARCs made of SiO_2 exhibit a Gaussian profile RI and register a peak transmission of 99.9% (up to 460 nm).[82] Moreover, a five layer (3 TiO_2 layers and 2 SiO_2 layers over it) by depositing atoms at 87° forms a GRIN film with quintically varying RI (resultant RI = 1.05) showing a minimum reflectivity of 0.1%[26] (Fig. 8(b)).

7.1.3. Chemical vapour deposition (CVD):. As the name suggests, this technique involves reaction and deposition of volatile precursor(s) on a heated substrate and it is one of the most widely used technique in the context of ARCs. In an effort to fabricate near-perfect optically absorbing materials, long (greater than 300 μm) and low-density (0.01–0.02 g cm^{-3}) vertically aligned carbon nanotubes (VA-CNTs) arrays have been produced by Yang *et al.*[83] using water assisted CVD. As is evident from Fig. 16(a), the total reflectance at 633 nm has been found to be an impressive 0.045%.

Plasma enhanced CVD (PECVD) is the most industrially preferred technology for Silicon Nitride anti-reflective coatings on crystalline solar cells, as we will see in section 10.[165]

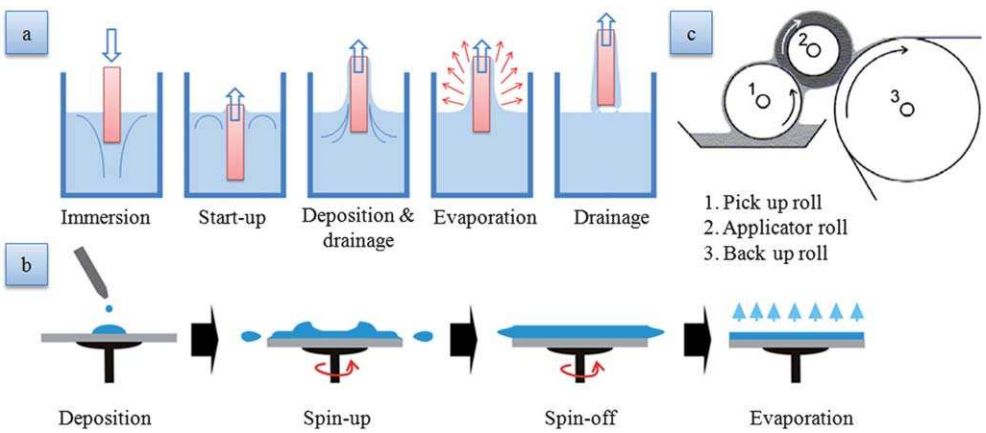

Fig. 14 Steps involved in (a) dip coating and (b) spin coating,[163] (c) technique of meniscus coating.[165]

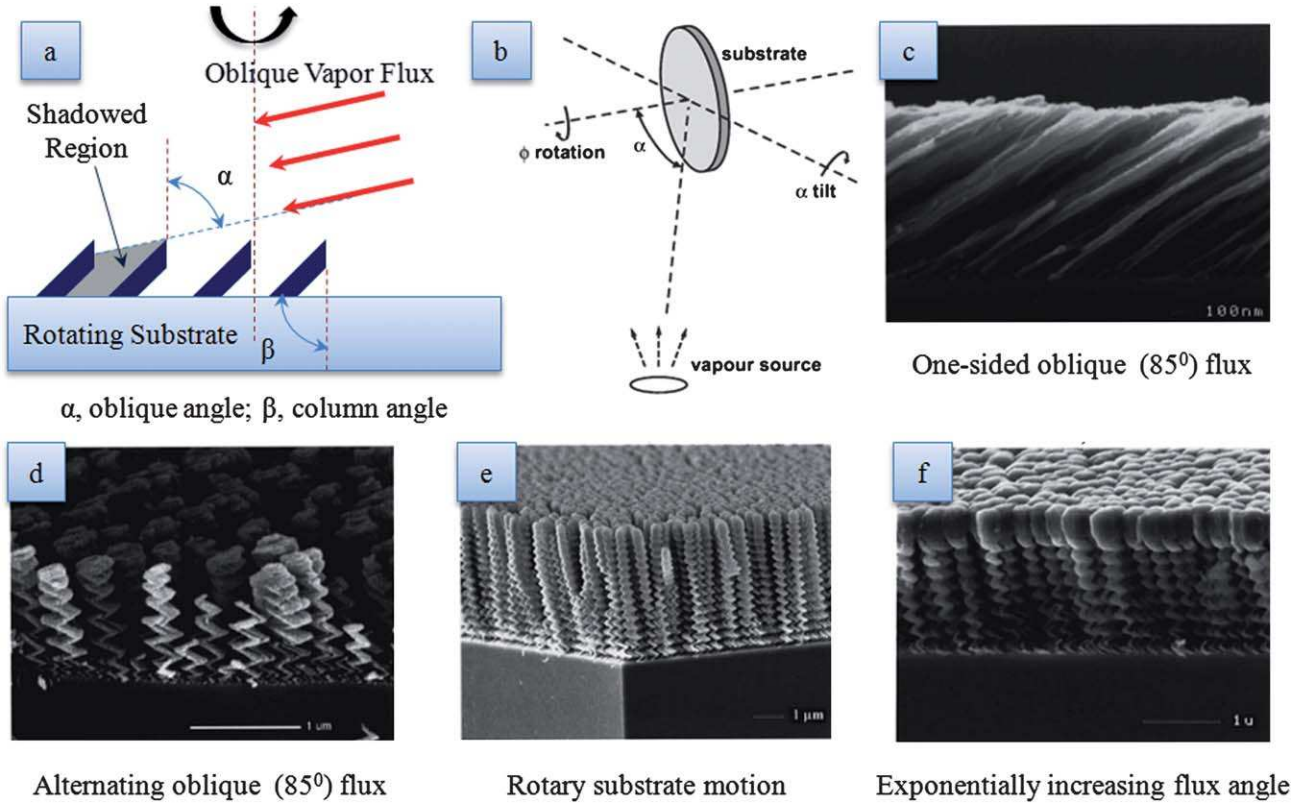

Fig. 15 (a) Schematic diagram of GLAD technique (b) modified GLAD to minimize the dependency between porosity and oblique angle,[79] (c) slanted microstructure,[84] (d) zigzag morphology,[84] (e) helix morphology,[84] (f) double MgF_2 layers with a capping MgF_2 layer.[84]

In fact, a multi-purpose coating[85,156] that combines anti-reflective, anti-scratch, easy-to-clean coating (of $SiO_xC_yH_z$ and TiO_2[85]) has been developed *via* PECVD and quite interestingly the coatings are tailor-made for polymers for example, PC (polycarbonate) and PMMA (polymethylmethacrylate).[85] In this technique the precursor molecules are decomposed by pulsed microwave-induced plasma and for instance, can have an adhesion layer followed by anti-reflective layer (TiO_2/SiO_2) and/or anti-scratch layer (SiO_2). Reflectance spectra[85] for the already discussed multi-purpose coating *via* PECVD displayed in Fig. 16 (b) shows that the anti-reflective coating produces a steady profile while the anti-scratch coating gives rise to fluctuations which the author logically attributes to the RI mismatch between the polymer substrate and the anti-scratch layer. The study also maintains that by using the PECVD technique the RI of the anti-scratch layer can be lowered to 1.46 thereby flattening the otherwise wavy reflectance *vs.* wavelength profile.

Radio frequency plasma enhanced CVD (RF-PECVD) has been reported to be effective in producing uniform coating for substrates of various shapes and sizes.[86] Diamond-like carbon (DLC) films having potential use in protective coating for IR windows and ARCs for solar cells have also been formed on Si substrate *via* RF-PECVD.[87] If we are to understand the performance of the film in real time solar applications such as solar collectors *etc.* the results bear significance for a temperature rise from 300 °C to 900 °C results in a change in reflectance from 8.75 to 18.27%, which brings into sharp focus the performance degradation of coatings under real-life conditions vis-à-vis temperature fluctuation.

Fabrication of GRIN RI is also feasible through atmospheric pressure CVD (APCVD) as shown by Neuman in his GRIN layer comprising the widely favoured SiO_2, TiO_2 duo[88] that has a reflectance of 0.5%. Quite interestingly analogous of nanostructures on *Morpho* butterfly wings[89] have been fabricated in the form of *Morpho* Christmas tree structures *via* focused ion beam CVD (FIB-CVD)[90] (Fig. 16(c)). However, the cost of covering even micrometres with this nanostructure is quite high whereas *Morpho* butterfly wings have these structures spread across many centimetres. This is just one of the numerous cues to be drawn from the exceptionally superior "nature". Apparently, the research on ARCs using CVD is quite exhaustive which is why a rather diverse perspective of ARCs using CVD and the techniques thereof is presented.

7.2. Conventional fabrication: top-down technology

7.2.1. Etching. Etching technique can be understood as a subtractive method that causes a selective dissolution or ablation of a surface or substrate in this case. Basically wet etching and dry etching are the two techniques relevant to our study and both processes are either mask-assisted or mask-less.

Wet etching quite obviously uses a chemical solution for the dissolution and is credited with advantages like precise selective attack and faster etching rate. To recount a study, Si AR SWS have been made by wet etching using single nanosized gold (Au) nobel particle as the catalyst.[91] The fact that structure and reflectivity of the Si surface is strongly affected by the shape and selection of material as the metal catalyst is the very reason why

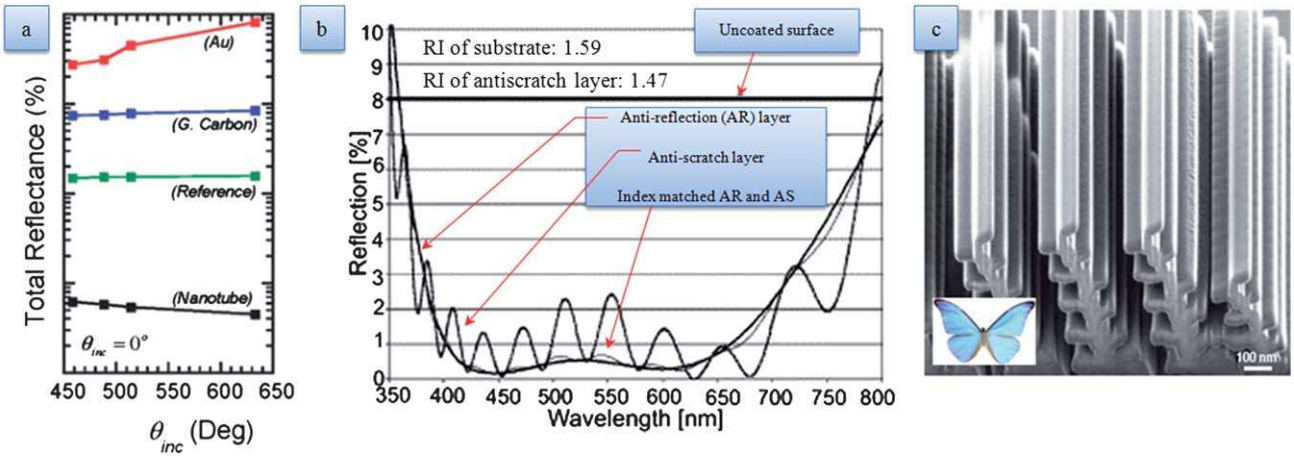

Fig. 16 (a) Comparative study of reflectance *vs* wavelength plots for VA-CNTs, glassy carbon (regarded as black body) and gold mirror.[83] (b) Reflectance spectra of PMMA with AR and AR + Anti-scratch coatings[85] *NB: The pointers and description have been modified for legibility*. (c) FIB-CVD fabricated mimic of nanostructures on "morpho" butterfly.[90]

Au is used for rather finer nanostructures. This can be understood by the idea that the size of each of the Au particle deposited on the surface of the substrate is determinant of the size of the grove that is produced after the Au particle is etched away from the surface. The state-of-the-art technique involves preheating so that Au particles attach on the substrate surface. This is followed by soaking of the substrate in aqueous solution of HF and H_2O and subsequently etching using catalysis of Au. A 15 min etched surface is this case bore a black appearance and registered a reflectance of less than 5% in 300–800 nm range.

Studies have also proved that *electrochemical etching* (in this category) of porous silicon, PSi is capable of adjusting the RI of PSi continuously without damaging the already formed PSi on Si substrate.[92] As the etching is performed at the interface (PSi–Si) the current density plays a decisive role in RI adjustment. The dynamic etching employed in this case has a steadily decreasing etching current density applied for less than 10 s. The reflectance plot also shows (Fig. 17(a)) reduction in reflectivity for PSi applied on *p*+ Si wafers and a simulation using a GRIN PSi layer, which in reality may be fabricated by applying a higher current density in the beginning imparting high porosity and then gradually decreasing the current density which will in turn lower the porosity, gives satisfyingly lower reflectance plots.

Dry etching is performed in vacuum chambers and surface removal is through ablation or volatilisation though plasma or ion bombardment. Surface texturing of Si that we discussed in the previous section also involves etching using femtosecond lasers[93–96,166] in the presence of SF_6 or N_2 and height of these spikes can be increased with increasing laser shots as starkly presented in Fig. 17 (b) (c).[166] In addition, the gas used while the etching is underway, say SF_6 or N_2 is quite an important factor as N_2 has proved to be less absorptive than SF_6 which shows appreciable performance in the IR region.[97] The scan speed of the laser determines the height and density of the spikes.[96] Fig. 17(d), (e) shows that microstructures in presence of SF_6 produce rather sharp tips as compared to blunt tips in presence of N_2. Moreover, the reflectance *vs* wavelength plot (Fig. 17(f)) also establishes the superiority of SF_6 which is mainly attributed to a combination of surface morphology, density and presence of surface defects (S and F in this case) that produce absorption states in the mid or the band edges of Si thereby increasing the absorption in NIR, thus, demonstrating the added advantage incorporating ARCs.

Chlorine trifluoride (ClF_3) gas has been used as a dry etchant to form honeycomb textured nanostructures on substrates[60,141,142] and it has been reported that ClF_3 gas can etch Si without plasma at temperatures near room temperature and doesn't affect SiO_2 or positive-type photoresist mask material.[63] Moreover, usage of ClF_3 doesn't hamper the isotropic property or crystal orientation of the substrate.

The corkscrew morphology of Si nanotips[99,143] explained in detail in the section *8.1* also employs a two step dry etching process. The technique is microetch mask assisted which can be etched away along with the substrate to produce the desired morphology. The first step is a reactive ion etching process (RIE) in the presence of CF_4 that produces Fluorine based compounds at random spots on the substrate. The second step is deep RIE which enhances the earlier "polymer-grass" like structure resulting in tall Si spike like structures (Fig. 21(h)).

7.3. Unconventional fabrication

7.3.1. Lithography. Patterning local surface of a substrate with nanoscale features can be performed by techniques such as scanning probe lithography (SPL), focused beam lithography (FBL) and nano imprint lithography (NIL) and being formed by a probe scanning the surface of the substrate, the features formed are self-assembled for the most part. In fact, NIL[100] has been demonstrated to have produced "moth's eye" structures on GaAs tandem solar cells.[101] First off, a replicated poly(vinyl chloride), PVC mold is fabricated by Hot Embossing on a Ni mold containing a hexagonal array of conical shaped structure with 300 nm pitch and height and diameter 300 and 250 nm, respectively. Next, this mold is lowered onto GaAs solar cells and placed in a pressurized imprinting system for replication on GaAs as shown in Fig. 18(a). The same technique has been used for texturing protective low iron glass of solar cells[102] and replicating SWS on large area polymer sheets.[103,104] NIL is also

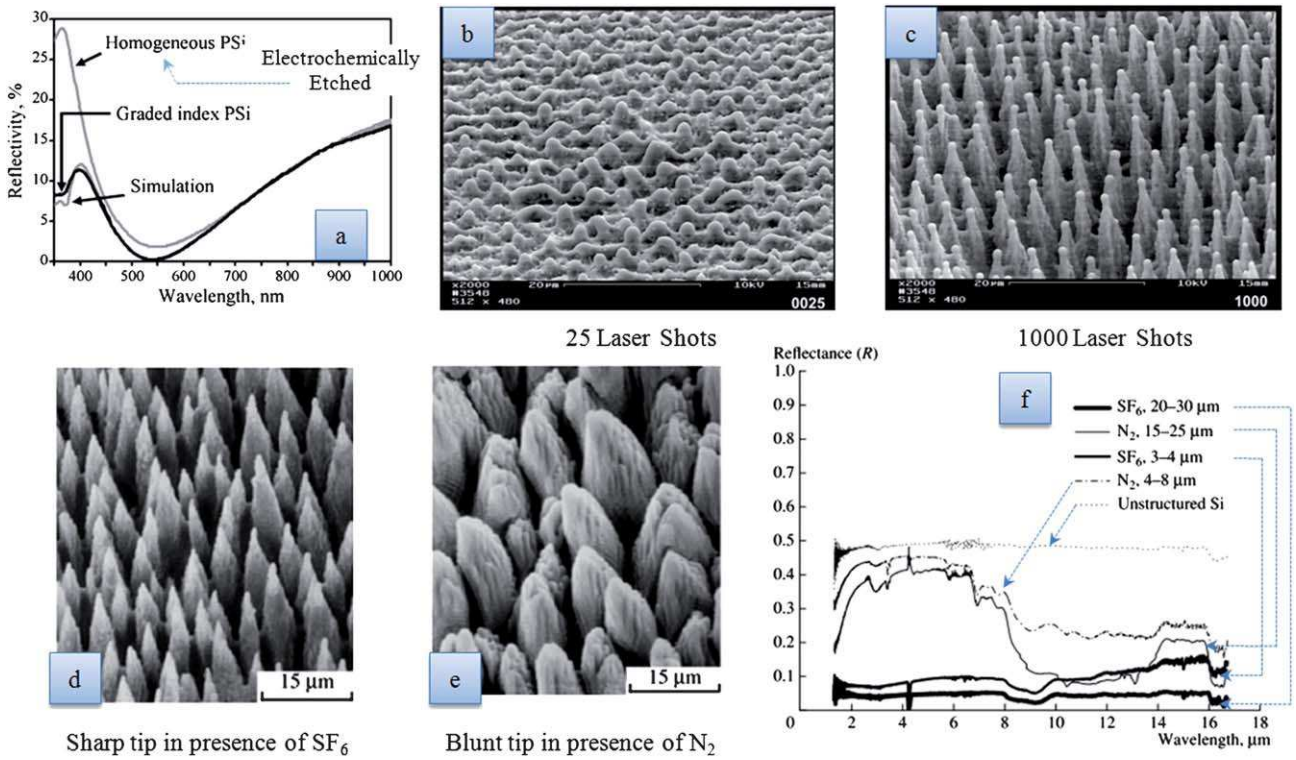

Fig. 17 (a) Reduction in reflectivity for PSi applied on p+ Si wafers confirming simulation profile.[92] (b) Surface texturing of Si showing height of the spikes at 25 laser shots and (c) 1000 laser shots.[166] (d) Tip profiles of spikes in presence of SF_6[98] (e) in presence of N_2.[98] (f) Reflectance *vs* wavelength plots for Si textured in the presence of SF_6 or N_2.[98] *NB: Pointers added to Fig. 17(f) for better understanding.*

the most preferred technique due to its low cost and high throughput advantages.

A study by Motamedi *et al.*[69] dealing with detectors that operate at long wavelengths (10–30 μm) and thus, might require thick ARCs which are susceptible to de-lamination during "repeated cycling to cryogenic temperatures" suggests pillar arrays on Si substrate by binary optics technology.[105] The nanostructure ensemble is fabricated using high-resolution lithography to transfer the micro-relief pattern onto the substrate followed by reactive-ion etching for appropriate depth and feature attainment. This enhances the transmission of the detector by approximately 90%.

7.3.2. Micro replication technique. Fig. 18 (c) explains the technique of roll-to-roll micro-replication process (R2R MRP) which entails replication of conical "moth's eye" nanostructures on thermoplastic polymer film, such as polyvinyl chloride (PVC) by host embossing.[106]

The master template made of polycarbonate has an array of conical moth's eye structures which when transferred to PVC film at 100 °C and 1 atm pressure, produces a tapered-hole pattern on PVC. This PVC template is in turn used to replicate the nanostructures on glass substrates. The interesting inference drawn in this study is that double side patterned glass shows a transmittance of 96% compared to 94% for one-sided. The most significant advantage of this technique is that it can be used to produce ARCs on wafer on a large scale. To enumerate the steps involved in the micro replication technique, it basically starts with an optical design with the help of an optical design applications.[108,144] This design is developed on a Si wafer through lithography and dry etching. The nanostructure pattern so developed on Si is then transferred onto a Ni mould by electroless plating which serves as the master template for all roll-to-roll micro replication done thereafter. This template when R2R is imprinted on a flexible PET surface produces the desired array of nanostructures on it.[106]

Bio template assisted micro replication techniques have also been reported. The surprisingly temperature resistant *cicadia* wings have been used in the replication process to fabricate large area AR SWS on polymethyl methacrylate (PMMA) polymer.[107] The authors of the research paper have quite illustratively explained the technique of replication (Fig. 18(b)). The *modus operandi* is a fabrication of a Au mould by depositing Au on *cicadia* wings thermally. The replica of the nanostructures so obtained on the Au template is in turn transferred to a PMMA film. An advantage of this technique is that the problem of PMMA sticking to the gold template doesn't arise which has been reasoned as the wax transmitted from the *cicadia* wings may have been transferred to the Au film.

7.3.3. Miscellaneous technique. *Photo-aligning*, *photo-patterning* which have been shown to have fabricated LCDs *etc.* has been reportedly employed[38] on optical polymer films that exhibit controlled surface topologies. The basic idea is that phase-separation can be induced optically in monomer liquid-crystal films on substrate such that nano-corrugated surface is generated on the surface. This monomer corrugation by phase separation of the polymer film produce uniform isotropic or

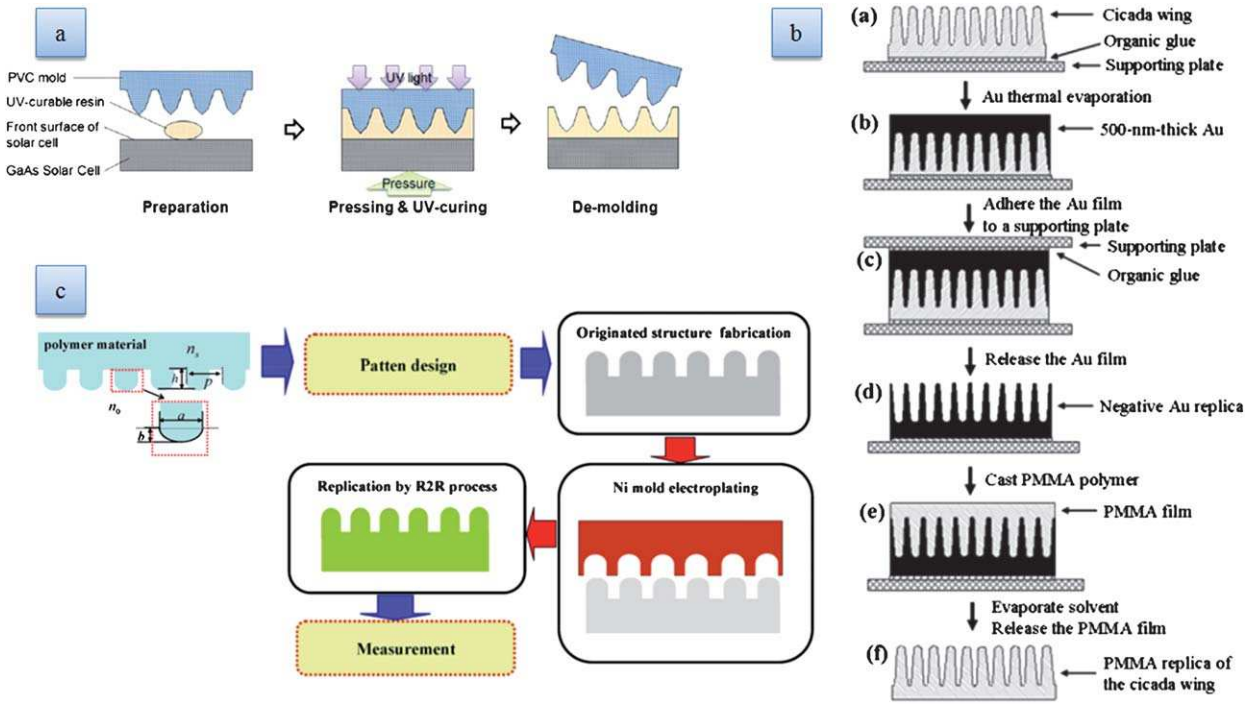

Fig. 18 (a) Flow chart of nano-imprint lithography technique producing "moth's eye" pattern on GaAs solar cells[101] (b) Stepwise bio-replication technique using cicadia wing as bio template[107] (d) Illustration of R2R MAP technique involving replication on PET.[106]

ansiotropic nanostructures and it can be used on a broader array of optical thin films. The results of applying the coating on glass surface is evident in the picture. Fig. 19 in one-sided and both-sided applications and the both-sided glass shows a very low reflectivity of 0.1% in the 400–700 nm wavelength zone, thereby maximizing the transmission to 99.1%.

8. The materials perspective of anti-reflectivity

8.1. Silicon based

Silicon is evidently one material that has been explored in all types of anti-reflective coatings, starting from porous silicon (PSi) on solar cells to Moth's eye inspired biomimetic structures and silicon nanotips. What makes it so indispensable is its use in the photovoltaic industry for reflection losses minimization and compatibility with Si photovoltaic.

A great many silica based ARCs especially the GRIN types have been looked at in the previous sections and it can be recalled that their exceptional hardness combined with very low RI (1.52005) makes them such an apt choice for ARCs. To bring PSi (Fig. 20(c)) back to our discussion, it has been reported that PSi has little or no angular dependency on reflectance even compared to ultrafast laser treated Si (Fig. 20(a)) with and without annealing and chemically textured Si (Fig. 20(b) with SiN_x[72] (Fig. 20(d)–(g)). It can also be observed in Fig. 20(g) that ultrafast laser textured sample which is thermally annealed has total internal scattering (TIS) values close to 100% which indicates non-absorption with energies less than the band gap and PSi and chemically textured Si samples also did not show any impressive TIS results validating the annealing effects on Si based ARCs (photon absorption reduced at higher temperature).

A quick relook at "biomimetics" ARCs also renders a slew of Si based nanostructure. Huang *et al.*[109] have fabricated a random array (packing density $\sim 6 \times 10^9$ cm^{-2}) of silicon nanotip structures having an apex diameter of $\sim$ 3–5 nm and a base diameter of $\sim$ 200 nm, length $\sim$ 1000–16000 nm by masked dry etching that reportedly outperforms the existing Si microstructures on the broadband and polarization-insensitivity counts. These SiNTs (Fig. 21(a),(b)) can be coated on wafers as demonstrated by this current study. However, SiNTs being dark arrays of nanostructures invoke curiosity with regard to their application on transparent optical devices or photovoltaic. Yet the study shows an impressive hemispherical reflectance (specular+diffuse) of 0.2% in 0.25–0.4 μm range and specular of less

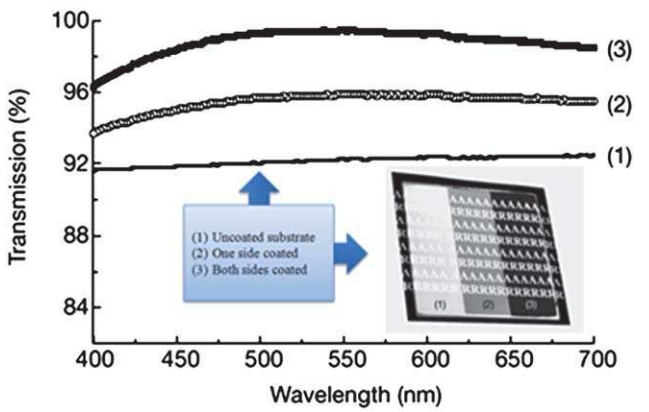

Fig. 19 Transmission *vs.* wavelength plot for a nano-corrugated surface on optical thin films by photo-aligning, photo-patterning. Notice the high glare in case of the uncoated film sample in (1).[38] *NB*: *Image modified by adding further information and images from the same paper for better understanding.*

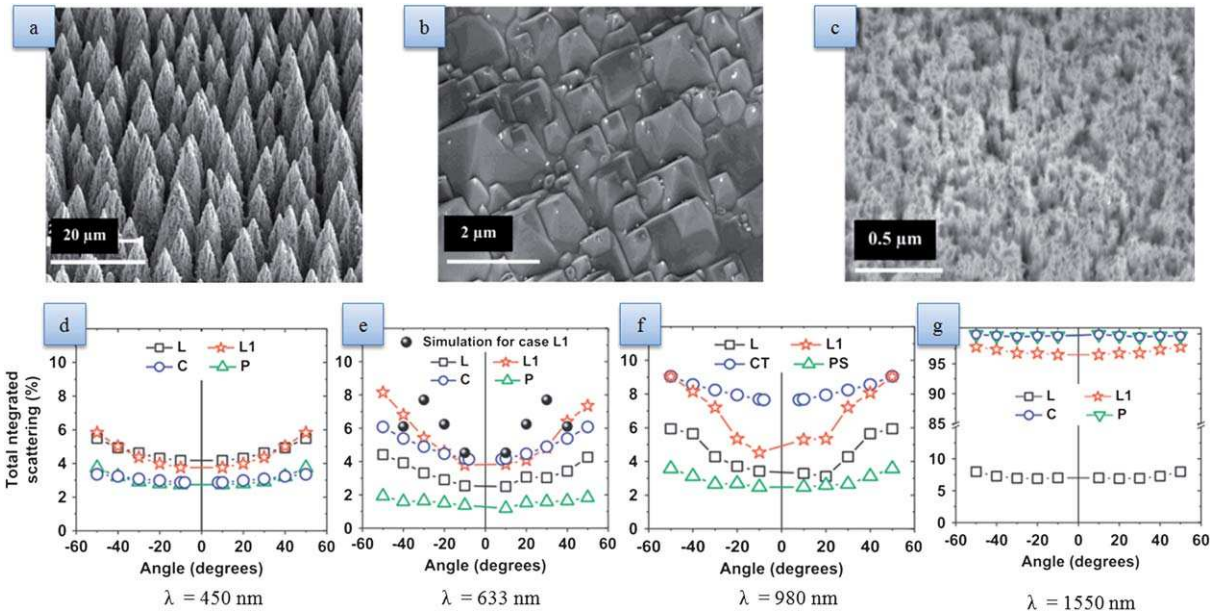

Fig. 20 (a) Ultrafast laser textured silicon surface in presence of SF_6 gas;[72] (b) chemically textured silicon surface;[72] (c) PSi surface;[72] (d)–(g) TIS *vs* angle plots at aforementioned wavelengths comparing ultrafast laser textured Si{L}, annealed ultrafast laser textured Si{L1}, chemically textured Si with SiN_x {CT}, Porous Si{P}.[72]

than 1% for 16 μm long SiNTs (Fig. 21(c),(d)). In fact, it can also be seen in Fig. 21(e),(f) that the performance of SiNTs is quite superior to Si wafers in case of s- and p-polarized lights and the fact that all the analysis encompassing the UV-VIS-NIR regions of the solar spectrum indicates the broadband properties of SiNTs as well.

In the THz regime (discussed above) SiNTs show quite an appreciable performance compared to other lithographically produced SWS, which can be attributed to the rather aperiodic or random arrangement of SiNTs as opposed to the other periodic arrays and hexagonally packed "moth's eye" nanostructures.

Similarly, Si nanopillar arrays by a self-assembly process involving self-assembled 2D polystyrene spheres as masks in reactive ion etching has been proposed by Xu *et al.*[110] Fig. 21(g) shows SEM image of these Si nanopillars which exhibit a reduction of reflectance in Si wafers from 32 to 8% and can be reduced to 1% in the 700–800 nm range. Although having a reduced reflectance, the Si nanopillars can be compared to the the SiNTs and the plateau in the former against the tapper in the latter and greater heights of SiNTs can conjure up a relationship between the effectiveness of ARCs and the tip profile and height/depth of the microstructures.

The fact that application of Si based ARCs has been reported in the aerospace industry and space exploration, just goes to show the diversity of its use. For instance, research undertaken[99,143] to establish a technique for minimizing ghost image formation on the micro sun sensors (MSS) for Mars Rover using Si nanotips is a case in point. It has been reported that Si nanotips, which have cork-screw morphology (Fig. 21(h)) coated with Cr/Au (to enhance absorption) at the target wavelength of 1m have 30° specular reflectance of the about 0.09% as opposed to 35% for bare Si and hemispherical reflectance is 8%. These AR when applied to the MSS helps correct the ghost image problem.

8.2. TiO_2 based

TiO_2 has been widely used as ARCs in silicon photovoltaics due to its matching refractive index (anatase 2.49, rutile 2.903) and low deposition cost. Numerous samples of ARCs using TiO_2 and TiO_2/SiO_2 multilayers, have already been given in the previous sections (6.2.3) and it is the RI of TiO_2 that can be used to lower the RI of glass slightly which eventually can be lowered further using SiO_2 mono or multi layers. However, one important aspect of TiO_2 worth mentioning here is that it doesn't facilitate substantial surface passivation which is desirable especially in semiconductors as it prolongs the effective life time of the charge career. This challenge has been squarely met by approaches[111,112,145,146] that involve initially growing a thin (5–30 nm) SiO_2 passivation layer and then depositing it with TiO_2.

8.3. Polymer based

Antireflective polymer optical films with SWS are a new area under exploration. Ting *et al.*[106] has reported a fabrication of periodic conical SWSs on flexible polyethylene terephthalate (PET) substrate using a nickel mould containing an array of cylindrical nanostructures. Fig. 22(a) shows a SEM image of the resulting nanostructure template containing conical and cylindrical array with a period of 400 nm, diameter 200 nm and height 350 nm. Reflectance and transmittance figures also stack up at 2.45 and 89.4% (450–700 nm range) respectively.

Surface porous polystyrene/poly(vinylpyrrolidone) (PS/PVP) polymer films by phase separation in a dip-coating process with precursors hydrophobic polystyrene (PS) and hydrophilic poly (vinylpyrrolidone) (PVP) at a volume ratio of 7 : 3 have been reported[113] to have tuneable film thickness, pore size and pore depth by altering the concentration of the PS/PVP solution and withdrawal speed during the fabrication. The films when applied

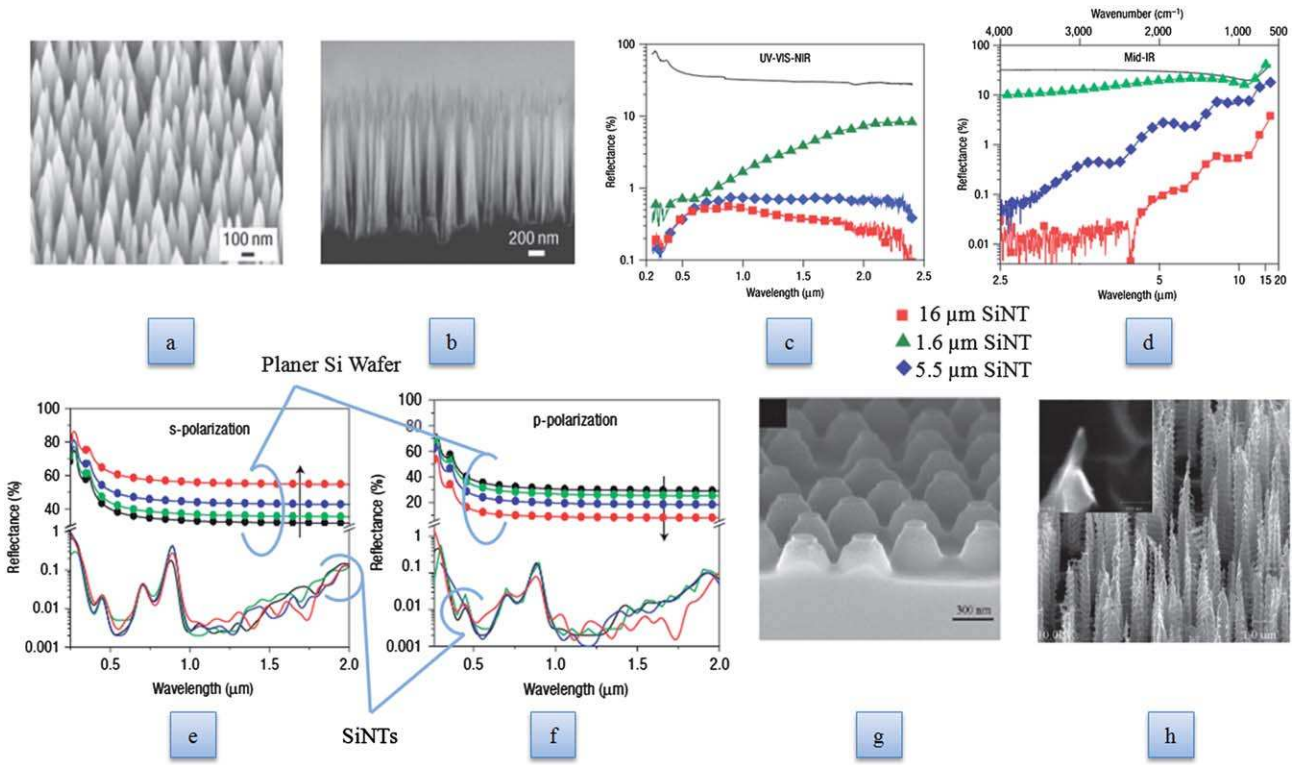

Fig. 21 (a) SEM image of 6-inch Si-NT wafer.[109] (b) Cross sectional SEM image of SiNT.[109] (c) Comparative study of hemispherical reflectance for Si wafer and SiNT[109] and (d) specular reflectance for Si wafer and SiNT, specular reflectance.[109] (e) Comparision of SiNTs w.r.t s-polarization;[109] (f) p-polarization of incident flux;[109] (g) SEM image of these Si nanopillars;[110] (h) corkscrew shaped Si nanotips[99] *NB: Markers added to Fig. 21(e) and (f) for better understanding.*

on glass surface reportedly increased the transmittance by 3–4% (Fig. 22(b)). Another paper reporting porous polymers based on self-assembled supramolecular block copolymer polystyrene terminated with carboxyl PS-COOH, poly(methyl methacrylate) terminated with amide (PMMA-NH_2)[114] demonstrated a 97.93% transmittance in visible wavelength range and on increasing the thickness from 152 to 203 nm, revealed an inhomogeneous 3 layered structure showing a transmittance of $\sim$ 99% when applied on both sides of glass.

Apart from these "moth's eye" structures fabricated on PMMA[115] with reflectance pegged at 1% and 4% when applied on one side and both sides of a glass substrate respectively and 2-D array of polystyrene spheres coated with Ag[116] are examples to show the growing interest in the field of polymer based anti-reflective coatings.

8.4. Gallium based

Group III–V semiconductors which by the virtue of their high career mobility and direct energy gaps are used in optoelectronics. Most of these materials pose broad band challenges due to their bandwidth disparity.

A survey of scientific works in this area uncovers mostly Gallium and Indium based ARCs. For instance, Random GaN nanopillars of 300, 550 and 720 nm height have been fabricated by *Chiu et al.*[117] GaN is a wide bandgap material (3.4eV) and has antireflective properties depending on structural roughness. The angle-dependent reflectance for *s*- and p-polarized light as showing in Fig. 23(a),(b) make it clear that the GaN nanopillars of 550 and 720 nm have similar profiles with reflectance at less than 3% up to 50°. Further analysis by RCWA reveals that the GaN nanopillars due to their cone-like or spearhead-like structure create a RI gradient (GaN, RI 2.5 to ambient) which contributes to the omnidirectional AR property. Similarly, random GaS based SWS have also been fabricated though Au mask etching and analyzed by *Leem et al.*[118] has been predicted to increase photonic absorption in GaAs based solar cells. The study also makes an insightful analysis of the reflectance and wavelength variation w.r.t etching time and an optimization of height and sidewall shape of the SWS led to a surface reflectance of less than 5% in the 350–900 nm range.

GaAs solar cells employing conductive Indium Tin Oxide (ITO) nanocolumns by the GLAD through electron beam have

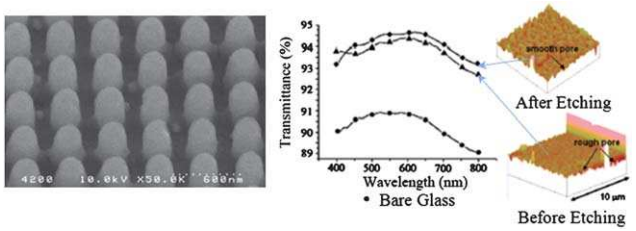

Fig. 22 (a) SEM image showing periodic conical nanostructures on PET.[106] [118] (b) Transmittance *vs* wavelength plot showing performance of surface porous PS/PVP before/after etching and glass.[113] *NB: Pointers added to Fig.22 (b) for better understanding.*

reported to have enhanced the efficiency of GaAs solar cells by 23%.[118] "Moth's eye" nanostructures have also been incorporated on GaAs tandem solar cells *via* nano imprint lithography[102] discussed in section 7.3.1. The reflectance without and with these nanostructures on GaAs solar cells are 14.34% and 9.08% as shown in Fig. 23(c).

Last but not the least, conically tapered GaP nanorods have been reportedly manufactured in the shape of "Moth's eye" nanostructures[119] and these serve as GRIN layers on the GaP substrate. Quite interestingly these nanostructures were fabricated by the vapour-liquid-solid (VLS) mechanism in a metallic organic vapour phase epitaxy (MOVPE) reactor. The growth of nanorods is facilitated by spin-coated gold particles on the substrate. According to the authors, temperature (570 °C) plays a crucial role in producing the desired conical morphology apart from the fact that the size of gold particles determines the base diameter of the cone during the vertical growth process. The transmission of the GaP substrate goes up by 15% due to this nanostructure ensemble especially registering a sharp absorption peak at GaP band-gap, 548 nm, as claimed by the study.

8.5. Carbon based

Amorphous diamond (a:DLC) like carbon films as hard AR coatings for Si solar cells [139] exhibit a transparency of 90% in VIS region and RI varying between 1.7 to 2.2 and even enable the solar cells to operate in oxide or corrosive environments. Additionally carbon nanotubes (CNTs) ARCs have been discussed in the section 7.1.3. The proverbial "moth's eye" nanostructure has been realized on the flat diamond surface[120] as well. The flat diamond surface has reflectance of around 18% at 10 μm. When this surface is replaced with the "moth's eye" structure the reflectance is reportedly reduced to 7% at the same wavelength values. The fabrication basically involves etching a reverse "moth's eye" onto Si by lithographic technique. Subsequently, diamond is grown on the etched surface by chemical vapour deposition and on dissolution of Si the leftover diamond assumes a moth's eye structure.

8.6. Organic based

Fatty acid films have been reported to have anti-reflective properties. Moreover they can act both as ARCs and protective shield for solar cells. Organic films of long chain fatty acids deposited by Langmuir–Blodgett (L-B)[121] technique on glass have been extended onto solar cells.[147] The L-B films administer control over their thickness, allows RI to be modified by changing the number of CH_2 groups or replacing H^+ with metal ions.

Intentional positioning of hydrophobic CH_3 on the outermost layer can impart hydrophobicity to the L-B film and photopolymerized polydiacetylene [$CH_3(CH_2)_n$ $-C\equiv C-C\equiv C-(CH_2)_m$–COOH] films inclusion can impart thermal and mechanical stability as studies[147] have proved. The research undertaken by Buckner *et al.*[122] uses stearic acid thin films (20–80 nm thick) coatings on Si solar cells by L-B technique shows that in 450–750 nm, organic films bring down the reflectance from 15% to 5–7% and in higher wavelength region, up to 5%.

9. Characterization techniques for anti-reflective coatings

The refractive index, reflectance and transmittance are the vital statistics that help deduce major inferences regarding the broadband, ominidirectional and polarization-insensitivity aspect of the ARCs. The optical characteristics of the films are examined using ex-situ ellipsometer and optical spectra measurements are done by UV-Vis-NIR spectrophotometer. In certain cases, crystallinity and orientation of the films are measured by high resolution X-ray diffractometer. Thickness and roughness measurements are done by the help of profilers such as Dektak stylus profiler. Chemical states, structures and composition are determined through X-ray photoelectron spectroscopy (XPS), Raman spectrometry and Fourier transform infrared spectroscopy (FTIR). All the images displaying topographical details and structural close-ups that we have seen so far are captured by the inevitable transmission electron microscopy (TEM), field emission scanning electron microscopy (FESEM) and atomic force microscopy (AFM). In a case where measurement of thermal conductivity of AR systems having diverse physical characters is required, the transient line heat source (TLHS) method is used. In addition, there is a large number of computational models that provide refractive index computing methodologies for different types of ARCs that we have discussed so far. These computational models relay on two of the

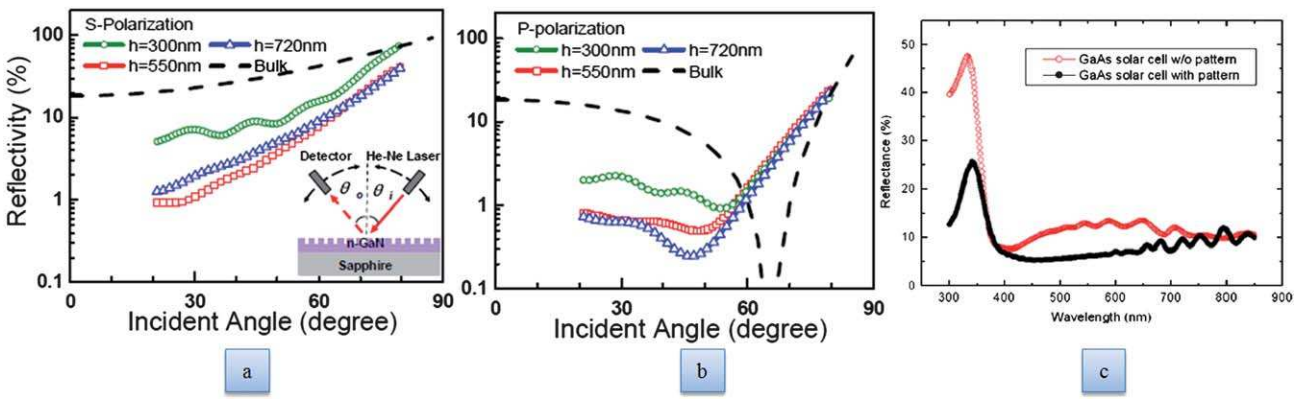

Fig. 23 (a) Reflectivty *vs* angle of incidence for GaN nanopillars subjected to s-polarized[117] and (b) p-polarized light.[117] (c) Reflectance *vs* wavelength for GaAs solar cells with and without patterns.[101]

already discussed landmark analytical techniques namely, the effective medium theory and the rigorous coupled wave analysis for refractive index computation. Durability of ARCs on solar panels can be judged by accelerated aging tests in real time condition. In fact, the accepted standards of adherence of coatings are supplied by US Military specifications MIL-C-675C, which involves MgF_2 anti-reflective coatings on glass substrates. Some of the stipulations of the same are presented here[123]

- The coating should not peel-off, crack or blister after being exposed to 95–100% humidity at 49 °C for 24 h or after being immersed in a sodium chloride solution (45 g L^{-1}) at room temperature for 24 h.
- Coating must withstand a 24 h salt spray fog test.
- Abrasions test involves a standard pencil eraser to be rubbed against the coated surface for 20 cycles (40 strokes) with a load of 10 N.
- Adherence test involves a cellophane tape to be pressed evenly and tightly to the coated substrate and removed quickly at an angle normal to the substrate.

10. Antireflective coatings on solar cells and modules

Besides numerous references to antireflective coatings on solar cells and enhancement in transmission by ARC in the previous sections, a focused discussion on ARC on solar cells and modules would bring forth the finer details such as the effect of encapsulants, cost-performance trade-off and accepted industry trends *etc.* and review the latest developments in this field.

The coating of antireflective layer on solar cells dates back to the 1960s when Elliot Berman observed that roughness on the wafer surface serves as a suitable ARC.[171] PV industry experimented with SiO_2 and TiO_2 ARC for some time though SiO_2 did not match optically (RI = 1.45) with the Si solar cell and TiO_2 despite being a better candidate for ARC did not contribute to surface passivation. Over the years continuous research has led to a notable industry trend—the application of silicon nitride (Si_3N_4) ARC instead of TiO_2 because the former is found to have excellent surface passivation properties. The Si_3N_4 coatings discourage carrier recombination at the surface of the solar cell which is highly desirable. Plasma enhanced CVD (PECVD) has been an industry approved fabrication technique for producing Si_3N_4 coatings on an N/P junction and it is this coating that imparts the dark blue color to the crystalline silicon solar cells. PECVD is a fast deposition technique and the deposition takes place at 400 °C[149,150] by the virtue of the following chemical reaction:

$$3\ SiH_4 + 4\ NH_3 \rightarrow Si_3N_4 + 24\ H_2$$

The by-product hydrogen (H_2) is used to accomplish the additional task of passivating the impurities and defects, a process better known as impurity-gettering (remove majority of the minority charge carriers).[148] Moreover, the nitride layer imparts a low resistance ohmic contact to the Ag-based contact metallization shown in Fig. 24(a). A well-designed layer for ARCs would be multipurpose if it has the following properties:[148]

1. Low reflectance over a broader solar spectrum
2. Low surface recombination velocity in case of a N^+/P solar cell
3. Provide a low ohmic resistance to the Ag-contact metallization
4. Encapsulate H_2 within the surface of Si and promote further diffusion to facilitate impurity-gettering

The optical property of the Si_3N_4 coating is of great interest and it has been reported that by lowering the proportion of Si in the film (RI as low as 1.9), the optical losses can be reduced since Si-rich film have higher refractive index and N-rich films have lower refractive index and our objective is to lower the RI to match the substrate RI.[148] A textured solar cell is deposited with a SiN_x:H coating, 750 Å thick. Fig. 24 (b) shows the calculated absorbance and reflectance of Si solar cell operating in air and the encapsulated module. However, in real time when the cell is encapsulated in ethylene vinyl acetate (EVA, RI = 1.5) an ARC of RI = 2.2 to 2 is found to be the optimum.[148] The reported calculated photocurrent density in the optimized coatings in case of solar cells and encapsulated module is 40.97 mA cm^{-2} and 39.74 mA cm^{-2}, respectively.

Kuo *et al.*[151] have designed an "all-λ – all-θ" AR design and fabricated the same by depositing layers of slanted nanorods layer-over-layer by means of glancing angle deposition (GLAD), producing seven layers with refractive index varying from 2.6 (near substrate) to 1.09 (adjacent to air) (Fig. 24(c)). This entire system can be treated as a gradient refractive index (GRIN) layer and the experimental reflectance data plotted in Fig. 24(d) shows a reflectance in the range of 1–6% (λ = 400–1600 nm) for all visible and near-infrared wavelengths. These multilayer coatings also exhibit a reflectance of 2–5% over a broad angle of incidence (0 to 60°) and they have reported that a transition from conventional coatings to the seven layers ARC on a Si wafer results in a solar-to-electric efficiency improvement from 20.5 to 42.7%.[151]

ARC coatings help in increasing the short-circuit current (I_{sc}) which translates into an increase in efficiency. The increase in I_{sc} is brought about by reduction in reflection at the front surface, absorption of base of photons closer to the collector junction and trapping the weakly absorbed photons within the cell for subsequent absorption.

The solar cells manufactured and characterized under ideal laboratory conditions stipulated by ASTM, AM 1.5 spectrums, perpendicular irradiance at 1000 W m^{-2} and temperature (25 °C) is not quite reflective of the real world conditions all the time and of all the geographies. Accurate thin film measurement also assumes paramount importance in the face of cost-efficiency trade-off. Spectroscopic ellipsometry (SE) provides a non destructive characterization technique by studying changes in polarization of light after being reflected from a layer on a solar cell.[152] SE measurement of nano-structured thin films is successful at wavelengths in the visible and higher regions. However, when textured silicon surface further coated with SiN_x is subjected to SE measurements, optical characterization poses a challenge because the reflected light from such surface is significantly less. This requires special techniques to collect adequate signals and from that model the interaction between the beam of light and individual rough surface.[152]

As we have already seen, solar modules have cells laid out between encapsulant sheets (typically EVA) the optical property

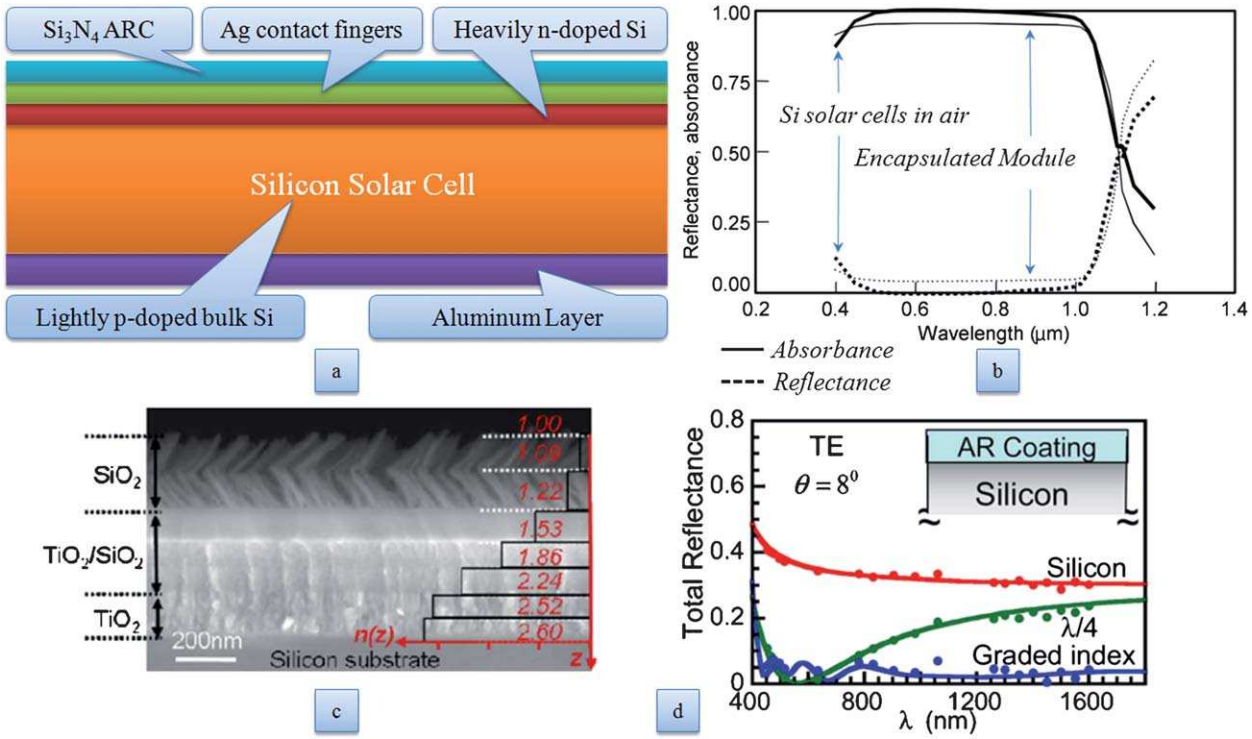

Fig. 24 (a) A typical silicon solar cell with the layer configuration displayed (b) calculated reflectance and absorbance in Si solar cell operating in air and encapsulated modules;[148] (c) scanning electron micrograph of gradient index ARC comprising seven layers;[151] (d) deduced experimental reflectance data from top surface of GRIN multilayer coating.[151]

of encapsulants also merits a discussion. The reflectance of SiNx coated cell (Fig. 25(a)), $R_{\text{cell/air}}$ or $R_{\text{cell/EVA}}$ is given by[154]

$$R = \left|\frac{m_{11}\tilde{n}_0 + m_{12}\tilde{n}_{si}\tilde{n}_0 - m_{21} - m_{22}\tilde{n}_{si}}{m_{11}\tilde{n}_0 + m_{12}\tilde{n}_{si}\tilde{n}_0 + m_{21} + m_{22}\tilde{n}_{si}}\right|^2$$

where

$$\begin{pmatrix} m_{11} & m_{12} \\ m_{21} & m_{22} \end{pmatrix} = \begin{pmatrix} \cos\delta_{SiNx} & \frac{i\sin\delta_{SiNx}}{\widetilde{n_{SiNx}}} \\ i\sin\delta_{SiNx}\widetilde{n_{SiNx}} & \cos\delta_{SiNx} \end{pmatrix}$$

and $\tilde{n}_i$ is the complex refractive index for the incident medium (can be used for air or EVA depending on presence or absence of encapsulant respectively) which can be written as $\tilde{n}_i = n_i - ik_i$ and $\delta_{SiNx} = \frac{2\pi d}{\lambda}\widetilde{n_{SiNx}}$. As complex refractive index has come into the reckoning, it's noteworthy that this consists of a real part which indicates the phase speed and an imaginary part which quantifies the amount of absorption loss. The imaginary part k is also called the extinction coefficient and if $k = 0$, light travels without any loss.

Grunow *et al.*[153] have measured the I_{sc} for an ecapsulated multicell as a function of the refractive index (RI) of SiN_x layer and its thickness. The results have confirmed the optimization parameters outlined by Doshi *et al.*[155] (RI 2.23, $\lambda = 68$ nm) and Ekai *et al.*[156] (RI 2.2, $\lambda = 67$ nm) and the optimum values of SiN_x coating on encapsulated solar cells is determined to be RI = 2.22 at $\lambda = 632.8$ nm and thickness of coating 67 nm (Fig. 25(b)). EVA and cell texturization for antireflective property have been analyzed in tandem by Grunow *et al.*[153] and the difference in reflectance between $R_{\text{cell/air}}$ and $R_{\text{cell/EVA}}$ is shown in Fig. 25(c). As the degree of texturization increases (0 to 50 to 100%) the difference in reflectance decreases though it comes at a decrease in encapsulation gain (EQE_{module}/EQE_{cell} where EQE is external quantum efficiency of a solar cell).

Pern *et al.*[157] have fabricated high quality single and bi-layer diamond-like carbon coatings for solar cells by two fabrication techniques, namely, ion-assisted plasma-enhanced deposition (IAPED) and electron cyclotron resonance (ECR) deposition. These DLC layers when deposited on Si or GaAs solar cells, serve as an antireflective coating (tunable RI from 1.5 to 2.6) and a protective encapsulant. The *I–V* (current–voltage) and *P–V* (power-voltage) graphs shown in Fig. 25(d) show that the DLC layer aids in efficiency improvement. Moreover, DLC layers are quite resistant to high humidity at high temperature, prevent moisture ingress and protect against mineral acids such as HCl, HNO_3 and H_2SO_4. These DLC films on Si wafers don't register any degradation in reflectance after having subjected to 762 h of rigorous damp-heat exposure[157] (85 °C and 85% relative humidity) and they don't peel-off and are highly scratch resistant.

As for the effectiveness of the ARCs on the front glass cover of the solar modules, a great deal of discussion has already been made and texturization and "moth's eye" nanostructure application have been discussed at length in the previous sections.

11. Contemporary research, challenges and conclusion

Anti-reflective coatings have been used in such diverse array of optical and optoelectronic devices such as lenses, eye-glasses

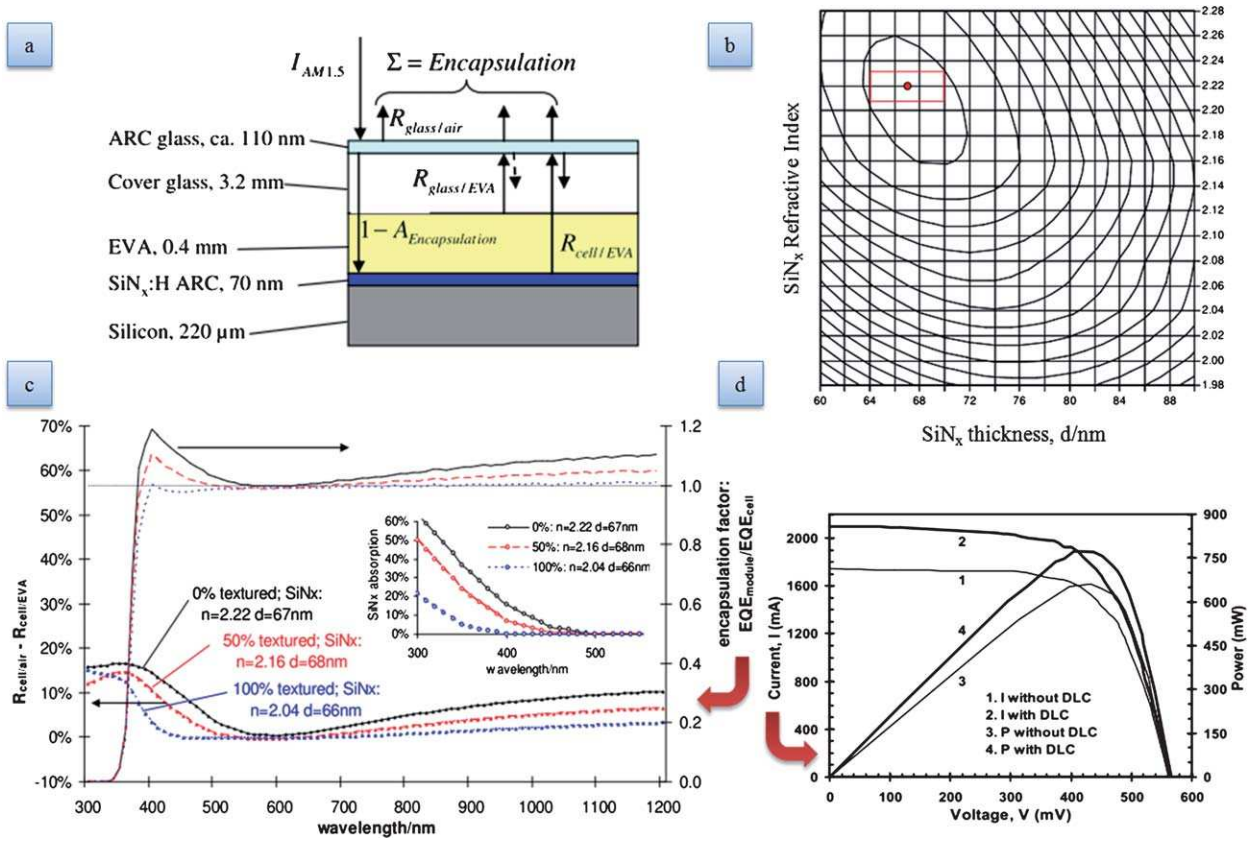

Fig. 25 (a) Encapsulated solar cell module with losses depicted at various layers;[153] (b) plot of short circuit current (I_{sc}) in an encapsulated multi-crystaline cell coated with SiNx antireflective coating;[153] (c) effect of the degree of texturization on the reflectance loss and encapsulation factor.[153] (d) Current–voltage and power-voltage curves for 100 cm^2 crystaline silicon solar cell.[171]

(Fig. 26(c)), military equipments, lasers, mirrors, solar cells, diodes, multipurpose narrow and broad band-pass filters, cathode ray tubes, television screens, sensors for aeronautical applications, cameras, window glasses and anti glare glasses for automotive applications (Fig. 26(c)) that the list is literally endless. Commercially, crystalline Si modules have all integrated anti-reflective coatings, self-cleaning coatings, encapsulant, one layer over the other on crystalline Si cells which is why there is this growing interest in fabricating hybrid coatings that serve as anti-reflective, self-cleaning, anti-microbial, low-emissivity coatings. Moreover, areas such as electrochromism and green architectural strategies have also led to the integration of ant-reflective property and electrochromism into one. The research on WO_3-TiO_2[124] composite films which are known for their electrochromic properties is one such example. Research on thermochromic AR materials is also underway.

Ensembles of "moth's eye" nanostructures have also been used in the anechoic chambers to reduce reflection of micro waves, wavelengths in the order of centimetres and millimetres.[123] As these chambers are used to measure radar reflections from test objects, radiations bouncing off the walls and causing distraction needs to be minimized. The coatings can be fabricated on a $Zr_{0.75}TiSn_{0.25}O_4$ ceramic microwave optical element of RI = 6. The coatings are mostly Al_2O_3 anti-reflection coatings with RI of 2.7 and thickness of 0.78 mm.[125]

As the Nobel Prize for Physics, 2010 marked the emergence of the ubiquitous, graphene, a lot of world-wide research effort has gone into exploring its applications. A recent report claiming an unprecedented feat of imaging graphene on gallium arsenide,[168] GaAs wafers is going to have far reaching impact on next generation semiconductors and optoelectronic devices. The crux of the matter is that the imagining is made possible by the use of an anti-reflective filter made of optimized layers aluminum arsenide on GaAs substrate. The reason why this is done is that when a very thin almost transparent layer (graphene) is super-imposed over another, the reflectivity of the underlying layer (5 layers of AlAs) will change prominently, *viz*. our very own concept of anti reflectivity.

A recent research on what is called inverse moth's eye of microwave or millimetre wavelength thickness has been reported by Mirotznik *et al.*[129] The fabrication technique is quite interesting in a way that they have suggested drilling multilevel sub-wavelength holes of various diameters as shown in Fig. 27 into a non-absorptive substrate and the modelling of the same relies on RCWA. The objective is to minimize reflectance in the 30 to 40 GHz broadband regime and from 0° to 60° angle of incidence. The grated multilayer hole array when formed on a Hik material, which has a dielectric permittivity of $\varepsilon_r = 9.0–0.02j$ shows 86% transmittance of incident power in the 32–38 GHz range. These are best candidates for passive imaging components where collection of more energy in the specified energy range and suppression of Fresnel reflections is of paramount importance.

Anti-reflective coatings have also been tested for their application on the new age organic solar cells which comprise many

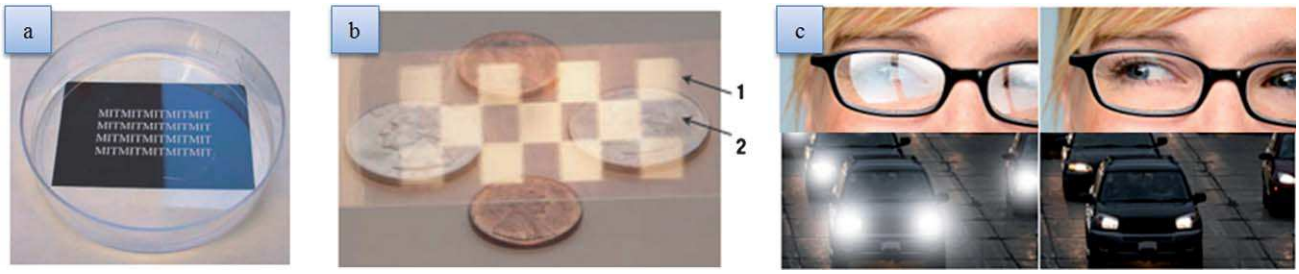

Fig. 26 (a) Polystyrene Petri dish half coated with PAH/PAA ARC. Notice the glare on the right half and the enhanced transparency in the left (b) patterned coatings showing 1-non-porous normal glass 2-anti-reflective zones.[127] (c) ARC reducing glare both from inside and outside in eye glasses and automobile glasses.[167]

layers. The organic solar cell made of glass/ITO/PEDOT has been shown to have minimized reflection losses by adding another layer of "moth's eye" nanostructure array and improving the performance of the cell by 2.5–3%.[126]

Reversibly erasable ARCs from polyelectrolyte PAH/PAA multilayer has also produced interesting results.[127] PAH/PAA multilayer have been repeatedly immersed in aqueous solution for not more than 5 min thereby alternating the value of n between 1.52 and 1.25 (non-porous to nano-porous). In anti-reflective state the reflectance is calibrated at 0.01% (650 nm). Fig. 26(a) shows the enhancement in transparency and reduction of glare brought about by using this ARCs on one side of a Petri dish. Additionally, patterned coatings with alternating anti-reflective spots, shown in Fig. 26(b) have been a potential application in microelectronic applications.[127] The drift from the conventional ARCs *vis-à-vis* this case is the fabrication technique which indeed is environment friendly. And this just goes to show that fabrication techniques of ARCs are undergoing major overhaul thereby offering immense opportunity for research and environmentally compatible technological innovation.

Anti-reflective coatings despite having exemplified their application in the field of solar photovoltaic still pose significant challenges with regard to their performance over a period of time. Pertinent among these is the issue of debonding or peeling-off of the ARCs applied not just on solar panels but eyeglasses too.

A research by Druffel *et al.*[128] on ceramic thin-films and polymer nanocomposites shows that the ceramic thin-films are susceptible to brittle fracture. Moreover, brittle materials will inherently exhibit features such as microcracks, crazings and voids *etc.* that serve as the origin of crack propagation. Humidity and difference in thermal coefficients at the interfacial zone (between film and substrate) can also lead to gradual peeling-off, what is otherwise technically known as debonding of the ARCs.

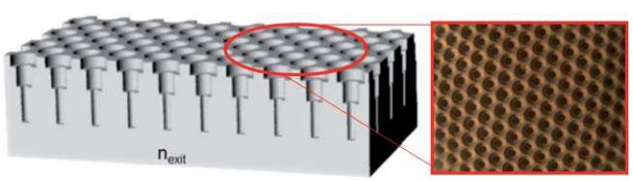

Fig. 27 Multilevel sub-wavelength gratings model forming reverse moth's eye (left) ARC and the same hole array structure machined on $12'' \times 12'' \times 0.5''$ slab of Hik material[129] *NB: Image modified slightly for better understanding.*

On the contrary, the materials that show higher propensity towards ductile fracture tend to exhibit durability but to survive the entire life of a solar cell with consistent performance is what calls for rigorous research and real-time testing of the anti-reflective coatings. In addition, most coatings are deposited at a stress range of 100–1000 MPa and residual stresses in the coating-substrate duo might set in due to disparity in thermal coefficients. If a coating of low thermal expansion is deposited on a substrate of high thermal expansion, due to higher contraction of the substrate than the coating, the coating is under tension and it results in a bend in the overall configuration as shown in Fig. 28(a) which is indeed exaggerated for better visualization. However, if the case is exactly the opposite that is, the coating has a higher thermal coefficient than the substrate the coating undergoes a contraction higher than the substrate which is why it tries to compress the substrate thereby bending it as shown in Fig. 28(b).

Besides, performance of the solar cell also gets impaired by accumulation of dust, microbes and moisture. The emergence of hydrophobic, hydrophilic and anti-microbial coatings based on the well known "lotus-effect" has facilitated integration of both the areas conceptualizing what is popularly known as "hybrid multi-purpose coatings". We have already seen examples of the same in the previous sections. Yet the trade-off between durability and affordability makes it really hard to strike a balance when it comes to formulating high efficiency anti-reflective coatings for solar cells at affordable price.

As for the materials, a particular family of materials called Reststrahlen materials which when exposed to radiation of wavelengths close to that which cause lattice vibrations in them, the Reststrahlen frequency is attained. These result in rapid change in the RI of the material, rise in extinction coefficient and sharp rise in Fresnel reflection coefficient as well. Thus, the reflectance increases sharply.[169] Dobrowolski *et al.*[19] in their quest for perfect anti-reflective materials have proposed a technique to reduce the reflectance in such materials. According to the computational study the lattice vibration might give rise to sharp absorption band and less than unity RI despite high extinction coefficient. A design of a 4-layer omnidirectional AR has also been proposed with substrate RI of 3.0 and it has been computed that for 7.2 μm wavelength the reflectance is 0.05 for all angels less than 85°.

A great deal of research on anti-reflective materials is underway as there are numerous unmet challenges some of which we discussed in the previous sections. More so because of the

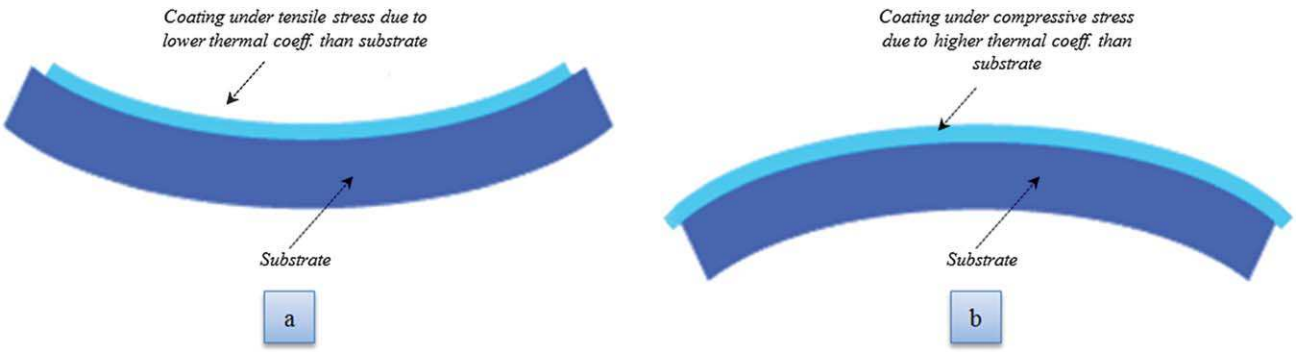

Fig. 28 Effect of thermal-coefficient mismatch between the coating and the substrate (a) thermal coefficient of the coating is less than that of substrate resulting in a concave bend (b) thermal coefficient of coating is higher than that of substrate resulting in a convex bend. *NB: Images exaggerated for better visualization.*

unprecedented surge in demand for highly efficient, durable and cost effective ARC for numerous optical and electronic equipments and to a greater extent for the solar cells as the paradigm shift to alternative sources of energy stands close to realization. New developments in optical devices also present immense opportunity for customization of anti-reflective coatings to suit the cutting edge technology and product improvisation. Last but not the least, the predominant biological aspect of anti-reflection is under close watch because of the intense biological research and findings confirming existence of even more sophisticated photonic nanostructures in many species (gyroids in butterflies, colossal eyes of squids *etc.*), which have to be explored in greater depth for their anti-reflective characteristics.

Acknowledgements

H.K.R and V.A.G thank National University of Singapore for graduate research fellowship. A.S.N and S.R thank the National Research Foundation, Singapore (Grant Number: NRF2007EWT-CERP01–0531) for partially supporting the program.

References

1 R. Hooke and F. o. t. R. Society, *Micrographia or some physiological descriptions of minute bodies*, Martyn and Allestry, London, 1665.
2 I. Newton and Thomas Jefferson Library Collection (Library of Congress), *Opticks: or, A treatise of the reflections, refractions, inflections and colours of light*, 4th edn, Printed for W. Innys, London., 1730.
3 A. R. Parker, *J. Opt. A: Pure Appl. Opt.*, 2000, **2**, R15–R28.
4 J. Fraunhofer, *Joseph von Fraunhofer Gesannekte Schriften*, Munich, Germany, 1888.
5 H. A. Macleod, *Thin-film Optical Filters*, 2nd edn, McGraw-Hill, 1989.
6 C. G. Bernhard, *Endeavour*, 1967, **26**, 79.
7 P. B. Clapham and M. C. Hutley, *Nature*, 1973, **244**, 281–282.
8 L. Schirone, G. Sotgiu and F. P. Califano, *Thin Solid Films*, 1997, **297**, 296–298.
9 A. Ramizy, W. J. Aziz, Z. Hassan, K. Omar and K. Ibrahim, *Microelectronics International*, 2010, **27**, 117–120.
10 H. G. Craighead, R. E. Howard, J. E. Sweeney and D. M. Tennant, *J. Vac. Sci. Technol.*, 1982, **20**, 316–319.
11 L. Rayleigh, *Proceedings of the London Mathematical Society*, 1879, s1–11, 51–56.
12 T. H. Elmer and F. W. Martin, *Ceram. Bull.*, 1979, **58**, 1092–1097.
13 J. C. M. Garnett, *Philos. Trans. R. Soc. London, Ser. A*, 1904, **203**, 385–420.
14 J. C. M. Garnett, *Philos. Trans. R. Soc. London, Ser. A*, 1906, **205**, 237–288.
15 D. A. G. Bruggeman, *Ann. Phys.*, 1935, **24**, 636–664.
16 J. A. Dobrowolski, *Optical properties of films and coatings in Handbook of Optics*, M. Bass edn, McGraw-Hill, New York, 1995.
17 Y. Fink, J. N. Winn, S. Fan, C. Chen, J. Michel, J. D. Joannopoulos and E. L. Thomas, *Science*, 1998, **282**, 1679–1682.
18 J. A. Dobrowolski and S. H. C. Piotrowski, *Appl. Opt.*, 1982, **21**, 1502.
19 J. A. Dobrowolski, D. Poitras, P. Ma, H. Vakil and M. Acree, *Appl. Opt.*, 2002, **41**, 3075–3083.
20 H. A. Macleod, *Thin Film Optical Filters* (Institute of Physics, Bristol, UK), 2001.
21 K. Q. Salih and N. M. Ahmed, *Int. J. Nanoelectron. Mater.*, 2009, **2**, 109–118.
22 J. T. Cox and G. Hass, *"Antireflection coatings for optical and infrared materials" in Physics of Thin Films*, Academic Press, New York, 1968.
23 Y. G. Kavakli and K. Kantarli, *Turk. J. Phys.*, 2002, **26**, 349–354.
24 W. H. Southwell, *Opt. Lett.*, 1983, **8**, 584–586.
25 B. Sheldon, J. S. Haggerty and A. G. Emslie, *J. Opt. Soc. Am.*, 1982, **72**, 1049–1055.
26 J. Q. Xi, M. F. Schubert, J. K. Kim, E. F. Schubert, M. Chen, S. Y. Lin, W. Liu and J. A. Smart, *Nature Photonics*, 2007, **1**(3), 176–179.
27 M. F. Schubert, D. J. Poxson, F. W. Mont, J. K. Kim and E. F. Schubert, *Appl. Phys. Express*, 2010, **3**, 082502–082503.
28 F. H. Nicoll and F. E. Williams, *J. Opt. Soc. Am.*, 1943, **33**, 434–435.
29 F. H. Nicoll, *J. Opt. Soc. Am.*, 1952, **42**, 241–241.
30 V. Lehmann and U. Gosele, *Appl. Phys. Lett.*, 1991, **58**, 856–858.
31 B. E. Yoldas and D. P. Partlow, *Thin Solid Films*, 1985, **129**, 1–14.
32 K. H. Jung, S. Shih, D. L. Kwong, C. C. Cho and B. E. Gnade, *Appl. Phys. Lett.*, 1992, **61**, 2467–2469.
33 R. Prado, G. Beobide, A. Marcaide, J. Goikoetxea and A. Aranzabe, *Sol. Energy Mater. Sol. Cells*, 2010, **94**, 1081–1088.
34 M. J. Minot, *J. Opt. Soc. Am.*, 1976, **66**, 515–519.
35 D. R. Uhlmann, T. Suratwala, K. Davidson, J. M. Boulton and G. Teowee, *J. Non-Cryst. Solids*, 1997, **218**, 113–122.
36 H. Hattori, *Adv. Mater.*, 2001, **13**, 51–54.
37 S. Walheim, E. Schäffer, J. Mlynek and U. Steiner, *Science*, 1999, **283**, 520–522.
38 M. Ibn-Elhaj and M. Schadt, *Nature*, 2001, **410**, 796–799.
39 W. H. Miller, C. G. Bernhard and A. R. Moller, *J. Opt. Soc. Am.*, 1964, **54**, 353.
40 A. R. Moller, C. G. Bernhard and W. H. Miller, *Acta Physiol. Scand.*, 1966, **S 68**, 140.
41 A. Yoshida, M. Motoyama, A. Kosaku and K. Miyamoto, *Zool. Sci.*, 1997, **14**, 737–741.
42 R. Brunner, A. Deparnay, M. Helgert, M. Burkhardt, T. Lohmüller and J. P. Spatz, Product piracy from nature: biomimetic microstructures and interfaces for high-performance optics

(Proceedings Paper): The Nature of Light: Light in Nature II, *SPIE*, 2008.
43 A. Sweeney, C. Jiggins and S. Johnsen, *Nature*, 2003, **423**, 31–32.
44 A. R. Parker and H. E. Townley, *Nat. Nanotechnol.*, 2007, **2**, 347–353.
45 M. Gale, *Physics World*, 1989, **2**, 24–28.
46 S. A. Boden and D. M. Bagnall, Photovoltaic Energy Conversion, *Conference Record of the 2006 IEEE 4th World Conference on*, 2006, **2**, 1358–1361.
47 A. R. Parker, Z. Hegedus and R. A. Watts, *Proc. R. Soc. London, Ser. B*, 1998, **265**, 811–815.
48 D. G. Stavenga, S. Foletti, G. Palasantzas and K. Arikawa, *Proc. R. Soc. London, Ser. B*, 2006, **273**, 661–667.
49 C. G. Bernhard, G. Gemne and J. Sällström, *Journal of Comparative Physiology A: Neuroethology, Sensory, Neural, and Behavioral Physiology*, 1970, **67**, 1–25.
50 R. C. Enger and S. K. Case, *Appl. Opt.*, 1983, **22**, 3220–3228.
51 H. Toyota, K. Takahara, M. Okano, T. Yotsuya and H. Kikuta, *Jpn. J. Appl. Phys.*, 2001, **40**, L747–L749.
52 W. L. Min, A. P. Betancourt, P. Jiang and B. Jiang, *Appl. Phys. Lett.*, 2008, **92**, 141109.
53 S. A. Boden and D. M. Bagnall, *Appl. Phys. Lett.*, 2008, **93**, 133108.
54 V. V. Iyengar, B. K. Nayak and M. C. Gupta, *Sol. Energy Mater. Sol. Cells*, 2010, **94**, 2251–2257.
55 B. Dale and H. G. Rudenberg, *Proc. 14th Annual Power Sources Conf.*, US Army Signal Research and Develeopement Lab., Ft. Monmouth, New Jersey, 1960, 22.
56 P. Campbell, *J. Opt. Soc. Am. B*, 1993, **10**, 2410–2415.
57 P. Campbell, *Sol. Energy Mater.*, 1990, **21**, 165–172.
58 A. W. Smith and A. Rohatgi, *Sol. Energy Mater. Sol. Cells*, 1993, **29**, 51–65.
59 Y. W. Chen, P. Y. Han and X. C. Zhang, *Appl. Phys. Lett.*, 2009, **94**.
60 P. Papet, O. Nichiporuk, A. Kaminski, Y. Rozier, J. Kraiem, J. F. Lelievre, A. Chaumartin, A. Fave and M. Lemiti, *Sol. Energy Mater. Sol. Cells*, 2006, **90**, 2319–2328.
61 J. Zhao, A. Wang, M. A. Green and F. Ferrazza, *Appl. Phys. Lett.*, 1998, **73**, 1991–1993.
62 B. L. Sopori, *Sol. Cells*, 1988, **25**, 15–26.
63 J. I. Gittleman, E. K. Sichel, H. W. Lehmann and R. Widmer, *Appl. Phys. Lett.*, 1979, **35**, 742–744.
64 Y. Saito and T. Kosuge, *Sol. Energy Mater. Sol. Cells*, 2007, **91**, 1800–1804.
65 Y. Wang, L. Chen, H. Yang, Q. Guo, W. Zhou and M. Tao, *Sol. Energy Mater. Sol. Cells*, 2009, **93**, 85–91.
66 D. M. Mittleman, *AIP Conf. Proc.*, 2005, **760**, 25–32.
67 M. Karlsson and F. Nikolajeff, *Opt. Express*, 2003, **11**, 502–507.
68 A. Gombert, K. Rose, A. Heinzel, W. Horbelt, C. Zanke, B. Bläsi and V. Wittwer, *Sol. Energy Mater. Sol. Cells*, 1998, **54**, 333–342.
69 C. Brückner, B. Pradarutti, O. Stenzel, R. Steinkopf, S. Riehemann, G. Notni and A. Tünnermann, *Opt. Express*, 2007, **15**, 779–789.
70 M. E. Motamedi, W. H. Southwell and W. J. Gunning, *Appl. Opt.*, 1992, **31**, 4371–4376.
71 W. H. Southwell, *J. Opt. Soc. Am. A*, 1991, **8**, 549–553.
72 H. Sai, H. Fujii, K. Arafune, Y. Ohshita, M. Yamaguchi, Y. Kanamori and H. Yugami, *Appl. Phys. Lett.*, 2006, **88**, 201116–201113.
73 C. J. Brinker and A. J. Hurd, *J. Phys. III*, 1994, **4**, 1231–1242.
74 H. Dislich and P. Hinz, *J. Non-Cryst. Solids*, 1982, **48**, 11–16.
75 E. K. Hussmann, *Key Eng. Mater.*, 1998.
76 H. G. Floch, P. F. Belleville, J.-J. Priotton, P. M. Pegon, C. S. Dijonneau and J. Guerain, *Am. Ceram. Soc. Bull.*, 1995, **74**, 60.
77 P. Hinz and H. Dislich, *J. Non-Cryst. Solids*, 1986, **82**, 411–416.
78 M. Faustini, L. Nicole, C. d. Boissieère, P. Innocenzi, C. m. Sanchez and D. Grosso, *Chem. Mater.*, 2010, **22**, 4406–4413.
79 K. Robbie, J. C. Sit and M. J. Brett, *J. Vac. Sci. Technol., B*, 1998, **16**, 1115–1122.
80 R. N. Tait, T. Smy and M. J. Brett, *Thin Solid Films*, 1993, **226**, 196–201.
81 R. Messier, T. Gehrke, C. Frankel, V. C. Venugopal, W. Otano and A. Lakhtakia, *J. Vac. Sci. Technol., A*, 1997, **15**, 2148–2152.
82 K. Robbie and M. J. Brett, *J. Vac. Sci. Technol., A*, 1997, **15**, 1460–1465.
83 S. R. Kennedy and M. J. Brett, *Appl. Opt.*, 2003, **42**, 4573–4579.
84 Z. P. Yang, L. J. Ci, J. A. Bur, S. Y. Lin and P. M. Ajayan, *Nano Lett.*, 2008, **8**, 446–451.
85 M. Kuhr, S. Bauer, U. Rothhaar and D. Wolff, *Thin Solid Films*, 2003, **442**, 107–116.
86 L. Martinu and D. Poitras, *J. Vac. Sci. Technol., A*, 2000, **18**, 2619–2645.
87 W. S. Choi and B. Hong, *Renewable Energy*, 2008, **33**, 226–231.
88 G. A. Neuman, *J. Non-Cryst. Solids*, 1997, **218**, 92–99.
89 S. Kinoshita, S. Yoshioka, Y. Fujii and N. Okamoto, *Forma 17*, 2002, **17**, 103–121.
90 K. Watanabe, T. Hoshino, K. Kanda, Y. Haruyama and S. Matsui, *Jpn. J. Appl. Phys.*, 2005, **44**, L48–L50.
91 S. Koynov, M. S. Brandt and M. Stutzmann, *Appl. Phys. Lett.*, 2006, **88**, 203107–203103.
92 C. C. Striemer and P. M. Fauchet, *Appl. Phys. Lett.*, 2002, **81**, 2980–2982.
93 C. Wu, C. H. Crouch, L. Zhao, J. E. Carey, R. Younkin, J. A. Levinson, E. Mazur, R. M. Farrell, P. Gothoskar and A. Karger, *Appl. Phys. Lett.*, 2001, **78**, 1850–1852.
94 J. D. Fowlkes, A. J. Pedraza and D. H. Lowndes, *Appl. Phys. Lett.*, 2000, **77**, 1629–1631.
95 T.-H. Her, R. J. Finlay, C. Wu, S. Deliwala and E. Mazur, *Appl. Phys. Lett.*, 1998, **73**, 1673–1675.
96 M. Zhao, G. Yin, J. T. Zhu and L. Zhao, *Chin. Phys. Lett.*, 2003, **20**, 1789–1791.
97 R. Younkin, J. E. Carey, E. Mazur, J. A. Levinson and C. M. Friend, *J. Appl. Phys.*, 2003, **93**, 2626–2629.
98 Y. Liu, S. Liu, Y. Wang, G. Feng, J. Zhu and L. Zhao, *Laser Phys.*, 2008, **18**, 1148–1152.
99 C. Lee, S. Y. Bae, S. Mobasser and H. Manohara, *Nano Lett.*, 2005, **5**, 2438–2442.
100 S. Y. Chou, P. R. Krauss and P. J. Renstrom, *Appl. Phys. Lett.*, 1995, **67**, 3114–3116.
101 K.-S. Han, J.-H. Shin, W.-Y. Yoon and H. Lee, *Sol. Energy Mater. Sol. Cells*, 2011, **95**, 288–291.
102 K.-S. Han, J.-H. Shin and H. Lee, *Sol. Energy Mater. Sol. Cells*, 2010, **94**, 583–587.
103 C. J. Ting, M. C. Huang, H. Y. Tsai, C. P. Chou and C. C. Fu, *Nanotechnology*, 2008, **19**, 205301.
104 Y. Kanamori, E. Roy and Y. Chen, *Microelectron. Eng.*, 2005, **78–79**, 287–293.
105 G. J. Swanson, *Binary optics technology: the theory and design of multi-level diffractive optical elements*, Tech. Rep. 854, Lincoln Laboratory, MIT, Lexington, Mass., 1989.
106 C. J. Ting, F. Y. Chang, C. F. Chen and C. P. Chou, *J. Micromech. Microeng.*, 2008, **18**, 075001.
107 G. Y. Xie, G. M. Zhang, F. Lin, J. Zhang, Z. F. Liu and S. C. Mu, Nanotechnology, 2008, 19.
108 T. K. Gaylord, W. E. Baird and M. G. Moharam, *Appl. Opt.*, 1986, **25**, 4562–4567.
109 Y.-F. Huang, S. Chattopadhyay, Y.-J. Jen, C.-Y. Peng, T.-A. Liu, Y.-K. Hsu, C.-L. Pan, H.-C. Lo, C.-H. Hsu, Y.-H. Chang, C.-S. Lee, K.-H. Chen and L.-C. Chen, *Nat. Nanotechnol.*, 2007, **2**, 770–774.
110 H. Xu, N. Lu, D. Qi, J. Hao, L. Gao, B. Zhang and L. Chi, *Small*, 2008, **4**, 1972–1975.
111 G. Crotty, T. Daud and R. Kachare, *J. Appl. Phys.*, 1987, **61**, 3077–3079.
112 B. S. Richards, J. E. Cotter and C. B. Honsberg, *Appl. Phys. Lett.*, 2002, **80**, 1123–1125.
113 C.-Y. Kuo, Y.-Y. Chen and S.-Y. Lu, *ACS Appl. Mater. Interfaces*, 2009, **1**, 72–75.
114 J. Gao, X. Li, B. Li and Y. Han, *Polymer*, 2010, **51**, 2683–2689.
115 A. Kaless, U. Schulz, P. Munzert and N. Kaiser, *Surf. Coat. Technol.*, 2005, **200**, 58–61.
116 P. Zhan, J. B. Liu, W. Dong, H. Dong, Z. Chen, Z. L. Wang, Y. Zhang, S. N. Zhu and N. B. Ming, *Appl. Phys. Lett.*, 2005, **86**, 051108–051103.
117 C. H. Chiu, P. Yu, H. C. Kuo, C. C. Chen, T. C. Lu, S. C. Wang, S. H. Hsu, Y. J. Cheng and Y. C. Chang, *Opt. Express*, 2008, **16**, 8748–8754.
118 J. W. Leem, J. S. Yu, Y. M. Song and Y. T. Lee, *Sol. Energy Mater. Sol. Cells*, 2011, **95**, 669–676.
119 S. L. Diedenhofen, R. E. Algra, E. P. A. M. Bakkers and J. G. Rivas, Next Generation (Nano) Photonic and Cell Technologies for Solar Energy Conversion, *Proc. SPIE–Int. Soc. Opt. Eng.*, 2010, **7772**, 77720M–77720M.

120 J. F. DeNatale, P. J. Hood, J. F. Flintoff and A. B. Harker, *J. Appl. Phys.*, 1992, **71**, 1388.
121 K. B. Blodgett and I. Langmuir, *Phys. Rev.*, 1937, **51**, 964.
122 S. L. Buckner and V. K. Agarwal, *Solar Energy Materials*, 12, pp. 131–136.
123 D. C. Harris, Materials for Infrared Windows and Domes: Properties and Performance, *SPIE*, 1999.
124 J. A. Hiller, J. D. Mendelsohn and M. F. Rubner, *Nat. Mater.*, 2002, **1**, 59–63.
125 E. O. Zayim, *Sol. Energy Mater. Sol. Cells*, 2005, **87**, 695–703.
126 P. Osbond, *Adv. Mater.*, 1992, **4**, 807–809.
127 K. Forberich, G. Dennler, M. C. Scharber, K. Hingerl, T. Fromherz and C. J. Brabec, *Thin Solid Films*, 2008, **516**, 7167–7170.
128 T. Druffel, K. B. Geng and E. Grulke, *Nanotechnology*, 2006, **17**, 3584–3590.
129 M. S. Mirotznik, B. L. Good, D. Wikner and J. N. Mait, Broadband Antireflective Properties of Inverse Motheye Surfaces, *IEEE Trans. Antennas Propag.*, 2010, **58**(9), 2969.
130 S. Bastide, M. Cuniot, P. Williams, N. Le Quang, D. Sarti and C. Levy-Clement, 12th EPSECE, Amsterdam, 1994, p. 4A25.
131 K. Grigoras, A. Krotus, V. Pacebutas, J. Kavaliauskas and I. Simkiene, *EMRS Conf Proc.*, Strasbourg, Elsevier, Amsterdam, 1995.
132 R. A. Arndt, J. F. Allison, J. G. Haynes, and A. Meulenburg Jr., *Prec. llth IEEE Photovoltaic Specialist Conf.* (IEEE New York, (1975) p. 40.
133 C. R. Baraona and H. W. Brandhorst, *Prec. llth IEEE Photovoitaic Specialist Conf.* (IEEE, New York, 1975) p. 44.
134 Prospect Glass ohne Reflexe. Deutsche Spezialglas AG, Grunenplan, FRG.
135 I. M. Thomas, *SPIE Proc. 2114*, 1993, 232.
136 I. M. Thomas, *Appl. Opt.*, 1986, **25**, 1481.
137 T. Kinoshita, K. Takahashi, T. Yanagisawa, M. Uehara, H. Kimata, US patent 5446339, Sumitomo Cement Co.
138 B. E. Yoldas, US Patent. No. 4271210, 1981.
139 C. E. Tracy, W. Kern, R. D. Vibronek, US Patent No. 4241108, 1980.
140 B. E. Yoldas, US Patent No. 4361598 and 4346131, 1982.
141 J. Zhao, A. Wang, M. A. Green, in: *Proceedings of the Second World Conference and Exhibition on Photovoltaic Solar Energy Conversion*, 1998.
142 O. Shultz, G. Emanuel, S. W. Glunz, G. P. Willeke, in: *Proceedings of the Third World Conference on Photovoltaic Solar Energy Conversion*, 2003, pp. 1360–1363.
143 H. Manohara, *NASA Tech Briefs*, vol. 28, (no. 11), pp. 62, November 2004.
144 S. Sinzinger, J. Jahns. (2003). *Microoptics*, 2nd edn Wiley-VCH, Weinheim (2003).
145 J. E. Cotter, B. S. Richards, F. Ferrazza, C. B. Honsberg, T. W. Leong, H. R. Mehrvarz, G. A. Naik, and S. R. Wenham, *Proceedings of the Second World Conference on Photovoltaic Energy Conversion*, Vienna, Austria, 6–10 July 1998, p. 1511.
146 R. M. Swanson, P. J. Verlinden, and R. A. Sinton, US Patent No.5,907,766, 1999.
147 D. BloorIn: J. Ladik, J. M. Angre and M. Seel, Editors, *Quantum Chemistry of Polymers—Solid State Aspects*, Reidel, Dordrecht (1984).
148 B. Sopori, Silicon nitride processing for control of optical and electronic properties of silicon solar cells, *J. Electron. Mater.*, 2003, **32**(10), 1034–1042.
149 K. Yasutake, Z. Chen, S. K. Pang and A. Rohatgi, Journal of, *J. Appl. Phys.*, 1994, **75**, 2048.
150 J. W. Lee, R. Ryoo, M. S. Jhon and K. I. Cho, *J. Phys. Chem. Solids*, 1995, **56**, 293.
151 M. Kuo, D. J. Poxson, Y. S. Kim, F. W. Mont, J. K. Kim, E. F. Schubert and S. Y. Lin, Realization of a near-perfect antireflection coating for silicon solar energy utilization, *Opt. Lett.*, 2008, **33**(21), 2527–2529.
152 J. N. Hilfiker, R. A. Synowicki, J.A., *Spectroscopic ellipsometry characterization: silicon-based solar cells*, Woollam Co., Inc., Photovoltaic International's 2nd Event Supplement.
153 P. Grunow, S. Krauter, Modelling the encapsulation factors for photovoltaic modules, *Proceedings of the 4th World Conference on Photovoltaic Energy Conversion (Joint congress of IEEE/PVSEC/ EUPVC)*, Waikoloa, Hawaii (USA), 12 May 2006.
154 O. S. Heavens, Dover Publications Inc. 1991.
155 P. Doshi *et al. IEEE Trans. Electron Devices 44*, 1997, p. 1417.
156 R. Ekai., *Proc. of the 2nd PV World Conference*, Vienna, 1998, 1430.
157 F. J. Pern, Zh. Panosyan, A. A. Gippius, J. A. Kontsevoy, K. Touryan, S. Voskanyan, Y. Yengibaryan, *Diamond-like carbon coatings as encapsulants for photovoltaic solar cells*, Nat. Renewable Energy Lab., Golden, CO, USA, Photovoltaic Specialists Conference, 2005. Conference Record of the Thirty-first IEEE, 3–7 Jan. 2005.
158 http://physicsworld.com/cws/article/news/37711/1/moth.
159 http://academic.udayton.edu/ShirleyWright/SEM/images/Samples/SEM_MothEye.jpg.
160 http://www.optida.lt/home.php?lng = EN&id = 249.
161 http://www.ultiquestcom.com/products/optics/coating_sar.html.
162 http://spie.org/x16144.xml?ArticleID=x16144.
163 http://www.csmonitor.com/Science/2010/0525/How-a-moth-s-eye-inspires-glare-free-TV-screens.
164 http://commons.wikimedia.org/wiki/File:SolGel_SpinCoating.jpg.
165 http://www.scielo.org.ar/scielo.php?pid=S0327-07932002000300006&script=sci_arttext.
166 http://www.crystec.com/triarce.htm.
167 http://mazur-www.harvard.edu/sentFiles/MazurTalk_382.pdf.
168 http://www.allaboutvision.com/lenses/coatings.htm.
169 http://www.eetimes.com/electronics-news/4084575/Graphene-mixes-it-up-with-GaAs.
170 http://www.crystran.co.uk/optics-definitions.htm.
171 http://en.wikipedia.org/wiki/Solar_cell.

